electrochem

MDPI

Article

Analytical–Computational Integration of Equivalent Circuit Modeling, Hybrid Optimization, and Statistical Validation for Electrochemical Impedance Spectroscopy

Francisco Augusto Nuñez Perez

Maestría en Ciencias en Ingeniería, Universidad Politécnica de Lázaro Cárdenas, Lázaro Cárdenas C.P. 60998, Michoacán, Mexico; augusto@uplc.edu.mx; Tel.: +52-1-753-136-4242

Abstract

Background: Electrochemical impedance spectroscopy (EIS) is indispensable for disentangling charge-transfer, capacitive, and diffusive phenomena, yet reproducible parameter estimation and objective model selection remain unsettled. Methods: We derive closed-form impedances and analytical Jacobians for seven equivalent-circuit models (Randles, constant-phase element (CPE), and Warburg impedance (ZW) variants), enforce physical bounds, and fit synthetic spectra with 2.5% and 5.0% Gaussian noise using hybrid optimization (Differential Evolution (DE) → Levenberg–Marquardt (LM)). Uncertainty is quantified via non-parametric bootstrap; parsimony is assessed with root-mean-square error (RMSE), Akaike Information Criterion (AIC), and Bayesian Information Criterion (BIC); physical consistency is checked by Kramers–Kronig (KK) diagnostics. Results: Solution resistance (R_s) and charge-transfer resistance (R_{ct}) are consistently identifiable across noise levels. CPE parameters (Q, n) and diffusion amplitude (σ) exhibit expected collinearity unless the frequency window excites both processes. Randles suffices for ideal interfaces; Randles+CPE lowers AIC when non-ideality and/or higher noise dominate; adding Warburg reproduces the 45° tail and improves likelihood when diffusion is present. The $(R_{ct} + Z_W) \parallel$ CPE architecture offers the best trade-off when heterogeneity and diffusion coexist. Conclusions: The framework unifies analytical derivations, hybrid optimization, and rigorous statistics to deliver traceable, reproducible EIS analysis and clear applicability domains, reducing subjective model choice. All code, data, and settings are released to enable exact reproduction.

Keywords: electrochemical impedance spectroscopy; equivalent circuits; constant-phase element; Warburg impedance; analytical Jacobian; hybrid optimization; bootstrap uncertainty; Kramers–Kronig; model selection; AIC/BIC

check for updates

Academic Editor: Gyözö G. Lang

Received: 19 August 2025
Revised: 22 September 2025
Accepted: 24 September 2025
Published: 8 October 2025

Citation: Nuñez Perez, F.A. Analytical–Computational Integration of Equivalent Circuit Modeling, Hybrid Optimization, and Statistical Validation for Electrochemical Impedance Spectroscopy. *Electrochem* **2025**, *6*, 35. https://doi.org/10.3390/electrochem6040035

Copyright: © 2025 by the author. Licensee MDPI, Basel, Switzerland. This article is an open access article distributed under the terms and conditions of the Creative Commons Attribution (CC BY) license (https://creativecommons.org/licenses/by/4.0/).

1. Introduction

Electrochemical impedance spectroscopy (EIS) is a frequency-domain technique that has become indispensable for the quantitative characterization of electrochemical interfaces and devices [1]. Unlike classical direct-current (DC) methods, EIS applies a small-amplitude sinusoidal perturbation and measures the resulting current response over several orders of magnitude in frequency, thereby resolving the interplay between resistive and reactive contributions at different characteristic timescales [2]. Operating under small-signal, linear time-invariant (LTI) conditions, EIS preserves the DC operating point while resolving concurrent faradaic (charge-transfer) and mass-transport phenomena across multiple decades of frequency via separation of characteristic time constants [3].

The complex impedance spectrum, $Z(\omega)$, encapsulates the system's dynamic response and can be interpreted by mapping it to an equivalent circuit model (ECM) in which each element corresponds to a specific physicochemical process [4,5]. Classical models, such as the Randles circuit, represent charge-transfer resistance (R_{ct}) in parallel with the double-layer capacitance (C_{dl}), in series with the uncompensated solution resistance (R_s) [6]. More advanced configurations incorporate non-ideal capacitive behavior via constant-phase elements (CPE) or account explicitly for semi-infinite diffusion through the Warburg diffusion impedance (Z_W), thereby extending the range of electrochemical systems that can be faithfully described [7].

Despite these advances, the recent literature still exhibits several unresolved limitations that hinder the reproducibility and reliability of EIS analysis: (i) the absence of a unified framework that integrates analytical derivation, robust parameter estimation, and statistical validation within a single workflow [8]; (ii) limited evaluation of model performance under controlled noise conditions, despite its direct relevance to experimental uncertainty [9]; (iii) scarce incorporation of Kramers–Kronig (KK) compliance testing as a systematic physical validity check [10]; and (iv) insufficient use of quantitative model selection criteria such as the Akaike Information Criterion (AIC) and the Bayesian Information Criterion (BIC) for objective discrimination among competing equivalent circuits. These gaps often lead to parameter estimates with low reproducibility and model choices driven by heuristic or subjective preference rather than rigorous, quantitative evidence [11].

In this context, an analytical–computational framework is proposed that unifies exact derivations of impedance functions for seven representative equivalent circuits with a hybrid fitting pipeline combining global and local optimization. The approach incorporates strict physical parameter bounds, analytical Jacobians for improved numerical stability, bootstrap-based uncertainty quantification, and automated validation against the Kramers–Kronig relations to ensure physical consistency. By systematically evaluating all models under controlled noise conditions, their statistical and physical domains of applicability are identified, thereby providing a reproducible methodology for rigorous EIS model selection.

Although equivalent-circuit models offer a convenient and widely adopted phenomenological representation of impedance data, they differ from physics-based approaches derived from transport and kinetic equations. While the latter provide parameters with a direct mechanistic interpretation, equivalent circuits mainly capture effective behaviors and may lead to over-interpretation if treated as physical constants. This distinction highlights the pedagogical value of the proposed framework: it clarifies the scope and limitations of phenomenological modeling while offering objective criteria for model selection.

1.1. Equivalent Circuit Foundations and Phasor Analysis

A rigorous interpretation of Electrochemical Impedance Spectroscopy (EIS) data demands an explicit understanding of how resistive, capacitive, and pseudo-capacitive elements interact within an equivalent circuit [12]. In this context, phasor analysis provides a compact mathematical framework that maps time-domain integro-differential relations into algebraic expressions in the frequency domain, enabling closed-form derivations of complex impedance functions [13].

Parallel Impedance Combination

For elements in parallel, the potential drop is identical across all branches, while the total current is additive [14]. This relation is elegantly expressed through the concept of admittance $Y = 1/Z$ [15], yielding the equivalent impedance:

$$Z_{\text{eq}} = \left(\sum_{k=1}^{N} \frac{1}{Z_k} \right)^{-1}, \tag{1}$$

where N is the number of parallel branches and Z_k is the impedance of branch k.

This formulation is central to archetypal EIS models, such as the Randles circuit, where the charge-transfer resistance (R_{ct}) and the double-layer capacitance (C_{dl}) or a Constant Phase Element (CPE) operate in parallel [16].

1.2. Charge-Transfer Resistance ($\boldsymbol{R_{ct}}$)

The charge-transfer resistance quantifies the kinetic barrier for electron transfer across the electrode–electrolyte interface. Unlike the solution resistance R_s, R_{ct} reflects interfacial phenomena and is modulated by electrode microstructure, activation energy, reactant concentration, and applied overpotential.

Linearization of the Butler–Volmer equation under small-signal perturbations ($\eta \ll$ 25 mV at 298 K) [17] leads to

$$R_{ct} = \frac{RT}{nFAj_0} \tag{2}$$

where R is the gas constant (J mol^{-1} K^{-1}), T temperature (K), n_e number of electrons transferred (dimensionless), F Faraday constant (C mol^{-1}), A active area (m^2), and j_0 exchange current density (A m^{-2}) establishing R_{ct} as a frequency-independent kinetic parameter [18]. In a Nyquist diagram, it is extracted from the mid-frequency semicircle diameter [19]:

$$R_{ct} = Z'(\omega \to 0) - Z'(\omega \to \infty) \tag{3}$$

These principles form the analytical backbone for the closed-form derivations presented herein, spanning from the classical Randles topology to advanced non-ideal and diffusion-impedance configurations, and directly supporting the quantitative model selection and validation framework developed in this work.

2. Equivalent Circuit Modeling and Analytical Simulation

The interpretation of Electrochemical Impedance Spectroscopy (EIS) data fundamentally relies on fitting equivalent circuit models, which represent physicochemical phenomena at the electrode–electrolyte interface using ideal and non-ideal electrical elements [20]. The primary components include the solution resistance R_s, associated with the ionic conductivity of the electrolyte, separators, and electrical contacts; the charge-transfer resistance R_{ct}, which quantifies the interfacial kinetics of the redox reaction; and the ideal double-layer capacitance C_{dl} [21].

The constant-phase element (CPE) is parameterized by Q and n, modeling a non-ideal capacitive behavior with impedance $Z_{\text{CPE}} = [Q(j\omega)^n]^{-1}$. To describe mass-transport phenomena, the Warburg impedance Z_W for semi-infinite diffusion is employed, defined as

$$Z_W(\omega) = \frac{A_W(1-j)}{\sqrt{2\omega}}, \tag{4}$$

where A_W has units $\Omega\,\text{s}^{-1/2}$.

Regarding impedance combination rules, in a series configuration the total impedance is $Z_{\text{total}} = \sum_i Z_i$, whereas in a parallel configuration it is obtained as $Z_{\text{total}} = (\sum_i Y_i)^{-1}$, where $Y_i = 1/Z_i$ denotes the admittance of the i-th element.

2.1. Series RLC (R–L–C)

The series RLC topology, comprising an ohmic resistor (R), an inductor (L), and a capacitor (C) connected in series, represents the canonical form of a lumped-element system with purely discrete resistive, inductive, and capacitive contributions. Although not directly descriptive of interfacial electrochemical processes, it constitutes a benchmark configuration for validating the analytical–computational methodology under controlled noise, owing to its closed-form solution and absence of distributed or diffusive elements [21,22].

The complex impedance is expressed as

$$Z_{\text{total}}(\omega) = R + j\omega L - \frac{j}{\omega C}, \tag{5}$$

where $\omega = 2\pi f$ denotes the angular frequency. The real and imaginary parts are

$$Z'(\omega) = R, \tag{6}$$

$$Z''(\omega) = \omega L - \frac{1}{\omega C}. \tag{7}$$

In the Nyquist representation, the spectrum collapses into a vertical line intersecting the real axis at R, with a positive imaginary component ($Z'' > 0$) in the inductive regime ($\omega \gg \omega_0$) and a negative imaginary component ($Z'' < 0$) in the capacitive regime ($\omega \ll \omega_0$). The resonant frequency,

$$\omega_0 = \frac{1}{\sqrt{LC}}, \tag{8}$$

marks the transition point where $Z''(\omega_0) = 0$ and the phase angle passes through 0°.

In the Bode magnitude plot, $|Z|$ exhibits a well-defined minimum at ω_0, corresponding to the cancellation of inductive and capacitive reactances. The Bode phase transitions monotonically from $+90^\circ$ (purely inductive response) at high frequency to -90° (purely capacitive response) at low frequency, with the ohmic contribution R governing the real-axis intercept in all regimes.

Relevance to this work: This idealized model provides a stringent test of the proposed fitting and validation framework, enabling direct assessment of numerical stability, parameter identifiability, and noise sensitivity without the confounding effects of dispersion or mass transport.

2.2. Classic Randles (R_s–[$R_{ct} \parallel C_{dl}$])

This circuit consists of R_s in series with the parallel combination $R_{ct} \parallel C_{dl}$, representing charge-transfer resistance coupled with an ideal double-layer capacitance. The impedance of the parallel branch is

$$Z_p(\omega) = \frac{R_{ct}}{1 + j\omega C_{dl} R_{ct}}. \tag{9}$$

Separating the real and imaginary components yields

$$Z'(\omega) = R_s + \frac{R_{ct}}{1 + (\omega C_{dl} R_{ct})^2} \tag{10}$$

$$Z''(\omega) = -\frac{\omega C_{dl} R_{ct}^2}{1 + (\omega C_{dl} R_{ct})^2} \tag{11}$$

Expected behavior: In the Nyquist plot, a perfect semicircle of diameter R_{ct} is obtained; in the Bode phase plot, a minimum occurs at $\omega_{\max} = 1/(R_{ct} C_{dl})$ (rad s^{-1}), equivalently $f_{\max} = \omega_{\max}/(2\pi)$ (Hz).

2.3. *Randles + CPE* (R_s–[$R_{ct} \parallel$ CPE])

Here, C_{dl} is replaced by a constant-phase element (CPE):

$$Z_{\mathrm{CPE}}(\omega) = \frac{1}{Q\,(j\omega)^n}. \tag{12}$$

where $0 < n < 1$ and Q has units $\mathrm{F\,s}^{n-1}$. The parallel branch impedance becomes

$$Z_p(\omega) = \frac{R_{ct}}{1 + R_{ct}Q(j\omega)^n}. \tag{13}$$

Effect: The Nyquist semicircle becomes depressed, with the degree of depression proportional to $(1 - n)$, indicating surface heterogeneity [23,24].

2.4. *Randles + Warburg* [$R_s + (R_{ct} \parallel C_{dl}) + Z_W$]

The *Randles + Warburg* configuration extends the classical Randles circuit by incorporating a semi-infinite diffusion element (Z_W) in series with the faradaic branch $R_{ct} \parallel C_{dl}$. This modification enables the simultaneous representation of charge-transfer processes and diffusion limitations that emerge at low frequencies in electrochemical systems governed by mass transport.

The total impedance is expressed as

$$Z_{\mathrm{total}}(\omega) = R_s + \left[\frac{1}{\frac{1}{R_{ct}} + j\omega C_{dl}}\right] + Z_W(\omega), \tag{14}$$

where $Z_W(\omega)$ denotes the semi-infinite diffusion Warburg impedance:

$$Z_W(\omega) = \frac{A_W(1-j)}{\sqrt{2\,\omega}}, \tag{15}$$

with A_W being the Warburg coefficient and ω the angular frequency.

Physical interpretation:

- R_s: ohmic resistance associated with the electrolyte and electrical contacts.
- R_{ct}: charge-transfer resistance at the electrode–electrolyte interface.
- C_{dl}: double-layer capacitance.
- Z_W: diffusive contribution describing the semi-infinite transport of reactive species.

In the Nyquist plot, this model produces a semicircle at intermediate frequencies (dominated by $R_{ct} \parallel C_{dl}$), followed by a diffusion tail with an approximate slope of 45° at low frequencies. In the Bode plot, the impedance magnitude exhibits a slope of -0.5 in the logarithmic scale at low frequencies, while the phase approaches $-45°$, which constitutes the characteristic signature of a semi-infinite diffusion [25].

2.5. $(R_{ct} + Z_W) \parallel C_{dl}$

In this model, the charge-transfer resistance R_{ct} and the semi-infinite Warburg impedance $Z_W(\omega)$ [25] (see Equation (4)) are connected in series before entering into parallel with the double-layer capacitance C_{dl}:

$$Z_{\mathrm{serie}}(\omega) = R_{ct} + Z_W(\omega) \tag{16}$$

$$Z_{\mathrm{total}}(\omega) = R_s + \left[\frac{1}{Z_{\mathrm{serie}}(\omega)} + j\omega C_{dl}\right]^{-1} \tag{17}$$

This topology is particularly relevant for systems in which mass transport of electroactive species is directly coupled to charge-transfer kinetics, such as in porous electrodes or materials with restricted ionic transport.

2.6. $(R_{ct} + Z_W) \parallel CPE$

This model is a variant of Model with R_{ct}, Z_W, and C_{dl}, in which the double-layer capacitance C_{dl} is replaced by a constant-phase element (CPE) [16] characterized by parameters Q and n. The semi-infinite Warburg impedance $Z_W(\omega)$ is defined as in Equation (4):

$$Z_{\text{total}}(\omega) = R_s + \left[\frac{1}{R_{ct} + Z_W(\omega)} + Q(j\omega)^n\right]^{-1} \tag{18}$$

Application: Suitable for describing rough or heterogeneous interfaces, as well as systems exhibiting a distribution of relaxation times where the diffusion of electroactive species is coupled to a non-ideal capacitive response.

2.7. Complete Randles (CPE + Warburg) $[R_s–[R_{ct} \parallel (CPE + Z_W)]]$

This is the most general topology considered in the present methodology, in which the constant-phase element (CPE) and the semi-infinite Warburg impedance [16,25] $Z_W(\omega)$ (see Equation (4)) are connected in series, and this branch is placed in parallel with the charge-transfer resistance R_{ct}, all in series with the solution resistance R_s:

$$Z_{\text{ser}}(\omega) = \frac{1}{Q(j\omega)^n} + Z_W(\omega) \tag{19}$$

$$Z_{\text{p}}(\omega) = \frac{R_{ct}\, Z_{\text{ser}}(\omega)}{R_{ct} + Z_{\text{ser}}(\omega)} \tag{20}$$

$$Z_{\text{total}}(\omega) = R_s + Z_{\text{p}}(\omega) \tag{21}$$

Application: This model simultaneously accounts for (i) non-ideal capacitive behavior due to surface heterogeneity or microscopic roughness, (ii) diffusive effects of electroactive species under semi-infinite transport conditions, and (iii) finite charge-transfer kinetics. It is particularly relevant for complex electrochemical systems such as composite electrodes, porous electrodes coated with non-uniform catalysts, and energy storage devices with coupled ionic and electronic transport.

Comparative Summary

Practical relevance: Models 1–2 are suited for systems dominated by charge-transfer processes with ideal or mildly non-ideal capacitive behavior (e.g., smooth metal electrodes, thin-film catalysts). Models 3–4 are appropriate for electrodes where diffusion plays a significant role, such as porous electrodes or systems with semi-infinite mass transport. Models 5–6 address scenarios with coupled charge-transfer and diffusion under non-ideal double-layer conditions, typical of heterogeneous, rough, or composite electrodes. Model 7 captures the most complex interplay of non-ideal capacitance, diffusion, and finite kinetics, enabling the most general representation of real electrochemical interfaces [26].

3. Methodology

A robust, fully modular computational platform was developed in Python 3.10.11 to simulate, fit, and validate electrochemical impedance spectroscopy (EIS) models with complete traceability and rigorous statistical control. The environment automates the entire simulate–fit–evaluate pipeline for seven equivalent circuit topologies, integrating hybrid

optimization, non-parametric bootstrapping, physicochemical consistency checks, and comprehensive visualization.

3.1. Analytical Model Definition and Jacobians

Each circuit is implemented as a complex impedance function $Z(\omega)$ in `NumPy`, together with its analytical Jacobian $\partial Z/\partial p_i$. The seven models considered are

(1) Series RLC: $Z = R + j\omega L + 1/(j\omega C)$
(2) Classical Randles: $R_s + (R_{ct} \parallel C_{dl})$
(3) Randles + CPE: $R_s + \left(R_{ct} \parallel [Q(j\omega)^n]^{-1}\right)$
(4) Randles + Warburg: $R_s + (R_{ct} \parallel C_{dl}) + \sigma/\sqrt{\omega}(1-j)$
(5) $(R_{ct} + Z_W) \parallel C_{dl}$
(6) $(R_{ct} + Z_W) \parallel \text{CPE}$
(7) Full Randles: $R_s + \left[R_{ct} \parallel \left(\frac{1}{Q(j\omega)^n} + \frac{\sigma}{\sqrt{\omega}}(1-j)\right)\right]$

Models are registered in a global `MODELS` dictionary exposing the impedance function, analytical Jacobian, parameter names, physical bounds, and initial relative scaling.

3.2. Synthetic Data Generation with Scaled Gaussian Noise

For each set of true parameters $\mathbf{p}_{\text{true}}$, a synthetic complex spectrum is generated and perturbed with additive Gaussian noise proportional to the impedance magnitude:

$$Z_{\text{exp}}(\omega) = Z(\mathbf{p}_{\text{true}}, \omega) + \varepsilon_i' + j\varepsilon_i'', \quad \varepsilon_i', \varepsilon_i'' \sim \mathcal{N}(0, \sigma_i), \quad \sigma_i = \frac{\alpha}{100}\,|Z(\omega_i)|$$

with controlled noise levels $\alpha \in \{2.5, 5.0\}\%$.

3.3. Multi–Stage Hybrid Fitting with Internal Scaling

The fitting routine `fit_impedance_data(...)` executes a robust two–stage optimization pipeline:

(a) **Global search:** $\chi^2(\mathbf{p})$ is minimized via differential evolution (`Differential Evolution`) over dimensionless scaled parameters, enforcing internal physical bounds.
(b) **Local refinement:** `Levenberg-Marquardt` (`least_squares`) is applied with analytical Jacobians, strict tolerances (xtol = ftol = gtol = 1×10^{-8}), and convergence verification.
(c) **Automatic scaling:** All parameters are normalized by an adaptive vector $\mathbf{s}$ derived from $\mathbf{p}_{\text{true}}$ or from physical limits, improving numerical conditioning.

Outputs include optimal parameters, complex residuals, evaluated Jacobian, and cost metrics.

3.4. Uncertainty Estimation via Parallelized Bootstrapping

A non-parametric bootstrap scheme with $N = 100$ resamples is executed in parallel (`multiprocessing`). Each resample is fitted from a neutral point in the scaled parameter space via `least_squares`:

$$\{\widehat{\mathbf{p}}^{(b)}\}_{b=1}^{N} \quad \Rightarrow \quad \text{CI}_{95\%} = \left[\text{percentile}_{2.5}, \text{percentile}_{97.5}\right]$$

3.5. Numerical Evaluation and Fit Diagnostics

Each converged fit is assessed using

Absolute error: RMSE over Z (both real and imaginary parts). Goodness-of-fit: χ^2, R^2, and adjusted R^2. Model complexity penalty: Akaike (AIC) and Bayesian (BIC) information criteria. Numerical conditioning: condition number of the Jacobian. Parameter correlations: correlation matrix from the pseudo-inverse of $(J^\mathsf{T} J)$, scaled by residual variance.

3.6. Systematic Exploration of Models and Noise Levels

For each model-noise combination $\{\text{model} \in [1,7], \alpha \in \{2.5, 5.0\}\}$, 50 independent fits are executed. The fit with the lowest RMSE is retained as the representative optimum. Final results are exported in both `CSV` and `JSON` formats for reproducibility and traceability.

3.7. Physical Validation and Automated Visualization

For each optimum fit, the system automatically:

(a) Generates Nyquist and Bode plots (magnitude and phase) plus residual plots.

(b) Performs Kramers–Kronig validation via the Hilbert transform of $\mathrm{Re}(Z)$. The reconstructed $Z''_{\mathrm{KK}}(\omega)$ is compared to the measured $Z''(\omega)$, and compliance is accepted if the relative deviation satisfies

$$\frac{|Z''_{\mathrm{KK}}(\omega) - Z''(\omega)|}{|Z(\omega)|} < 0.05$$

for all frequencies, corresponding to a 5% tolerance.

(c) Exports graphical data in `CSV` and all associated parameters and metrics in `JSON`.

4. Results

The series RLC model was evaluated at 2.5% and 5.0% noise levels. Each figure uses subpanels (a) 2.5% and (b) 5.0%; in-text citations appear as Figure Xa and Figure Xb (e.g., Figure 1a,b, Figure 2a,b, Figure 3a,b, Figures 4a,b and 5a,b).

In the Nyquist diagram (Figure 1a,b), both noise levels reproduce the model's characteristic arc, with the 5.0% case exhibiting greater scatter in the high-frequency region. Nevertheless, the fitted curves remain in close agreement with the simulated spectra.

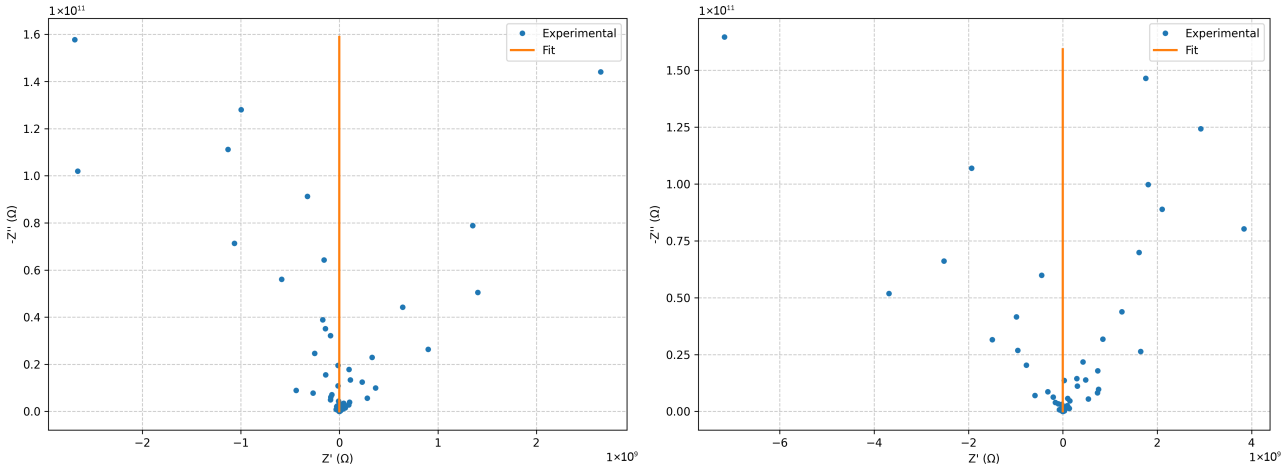
The Bode magnitude (Figure 2a,b) shows excellent fidelity across several frequency decades, with only minor deviations at 5.0% noise in the high-frequency limit. The Bode phase (Figure 3a,b) reproduces the expected phase profile without significant distortion from noise.

The residuals, defined as raw complex differences $r_i = Z_{\mathrm{exp}}(\omega_i) - Z_{\mathrm{fit}}(\omega_i)$, are shown in Figure 4a (2.5%). They remain centered and nearly homoscedastic. In Figure 4b (5.0%), variance increases proportionally to the noise level, yet no systematic bias emerges, indicating the robustness of the fit.

Kramers–Kronig validation via the Hilbert transform (Figure 5a,b) confirms the causality, linearity, and stationarity of the fitted spectra at both noise levels, with no significant violations.

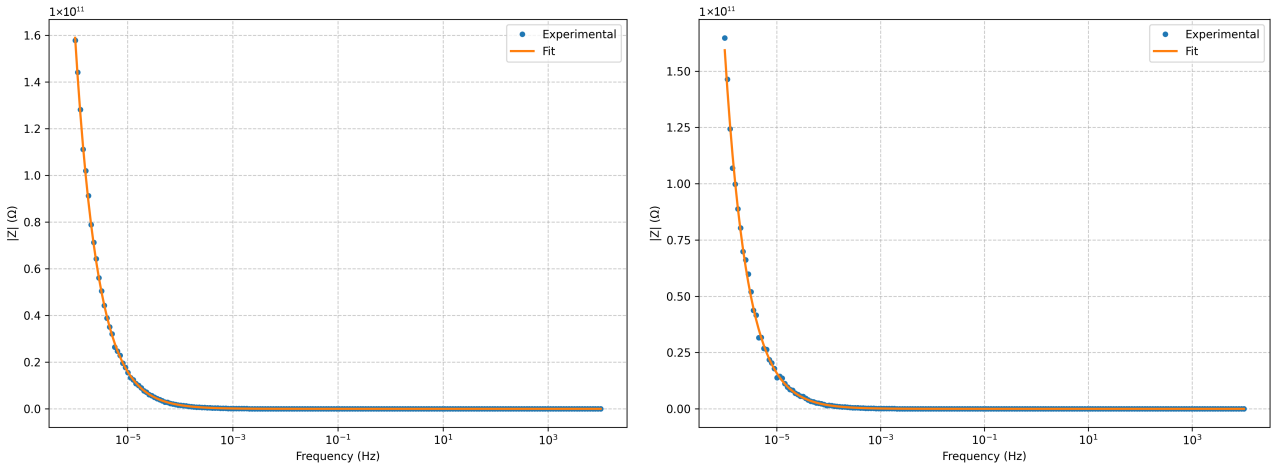
The quantitative summary in Table 1 shows R^2 and adjusted R^2 values exceeding 0.997 in all cases, with fitted parameters lying within narrow 95% confidence intervals around nominal values. Increasing the noise from 2.5% to 5.0% causes modest increases in RMSE, χ^2, AIC, and BIC, as well as slight variations in R, L, and C, without compromising the model's validity.

Overall, the series RLC model demonstrates high stability and predictive reliability under moderate noise, preserving both statistical robustness and physical consistency.



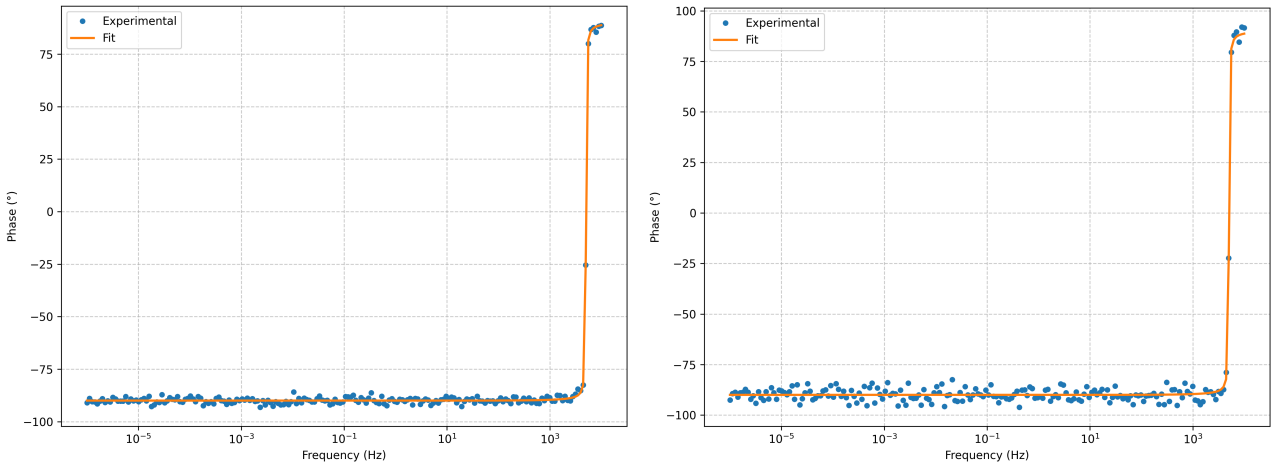
(**a**) 2.5% (**b**) 5.0%

Figure 1. Nyquist diagrams for the series RLC model: comparison between 2.5% and 5.0% noise.



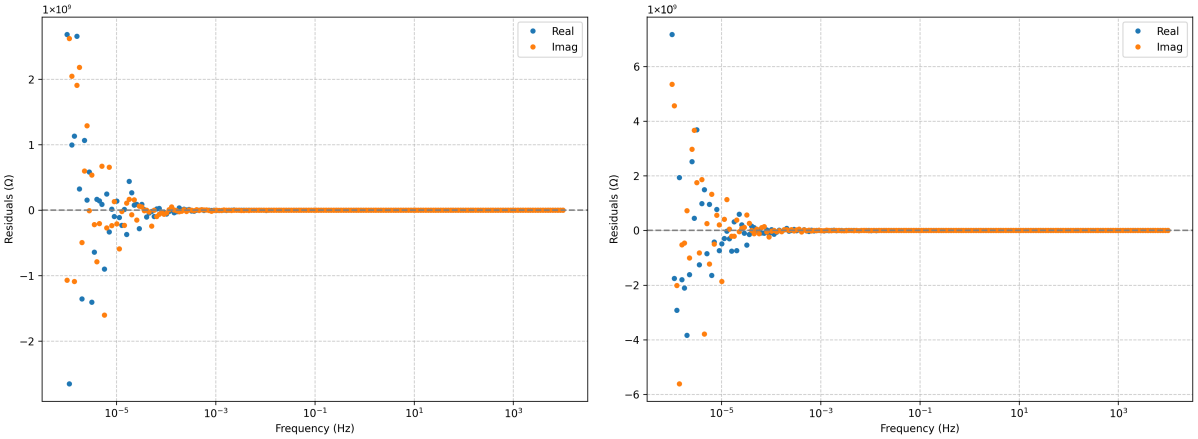
(**a**) 2.5% (**b**) 5.0%

Figure 2. Bode magnitude for the series RLC model at 2.5% and 5.0% noise.



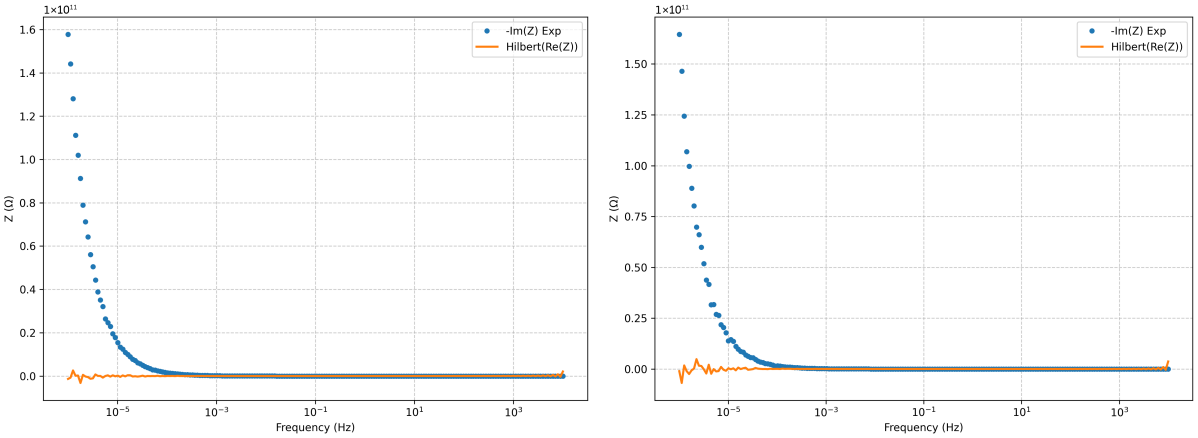
(**a**) 2.5% (**b**) 5.0%

Figure 3. Bode phase for the series RLC model at 2.5% and 5.0% noise.



(**a**) 2.5% (**b**) 5.0%

Figure 4. Raw complex residuals $r_i = Z_{\text{exp}} - Z_{\text{fit}}$ (real and imaginary parts) for the series RLC model: (**a**) 2.5% noise; (**b**) 5.0% noise.



(**a**) 2.5% (**b**) 5.0%

Figure 5. Kramers–Kronig validation (Hilbert transform) for the series RLC model.

Table 1. Summary of metrics and parameters for series RLC (best fit at each noise level).

	2.5%	**5.0%**
RMSE	5.494×10^{8}	1.152×10^{9}
χ^2	3.494×10^{2}	4.018×10^{2}
R^2	9.9947×10^{-1}	9.9767×10^{-1}
R^2_{adj}	9.9946×10^{-1}	9.9766×10^{-1}
AIC	4×10^{2}	4×10^{2}
BIC	4×10^{2}	4×10^{2}
Cond#	4.6×10^{1}	4.6×10^{1}
R [Ω]	1.000 [0.991, 1.295]	1.061 [0.514, 1.257]
L [mH]	0.999 [0.994, 1.006]	1.002 [0.982, 1.010]
C [µF]	1.002 [0.999, 1.005]	0.999 [0.992, 1.005]

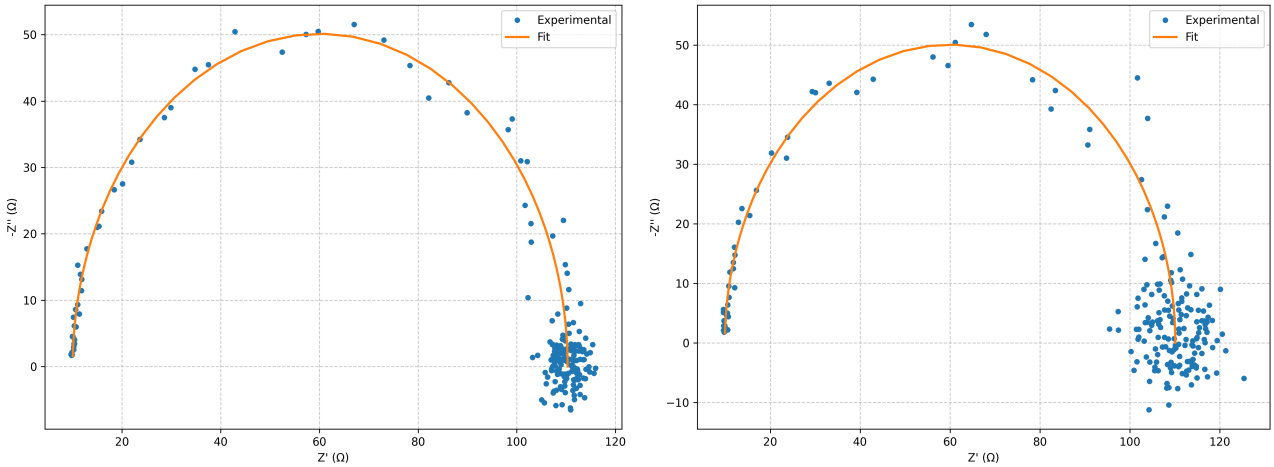
Values in brackets: 95% confidence intervals. L rescaled to mH and C to µF for clarity. Bold entries (RMSE, AIC, BIC, Cond#, and circuit parameters) indicate the key fitting metrics and estimated model parameters highlighted in the discussion.

4.1. Model: Classic Randles $R_s + (R_{ct} \parallel C_{dl})$

The classic Randles model was evaluated under controlled noise levels of 2.5% and 5.0%. In both cases, the characteristic semicircle appears slightly depressed due to discrete

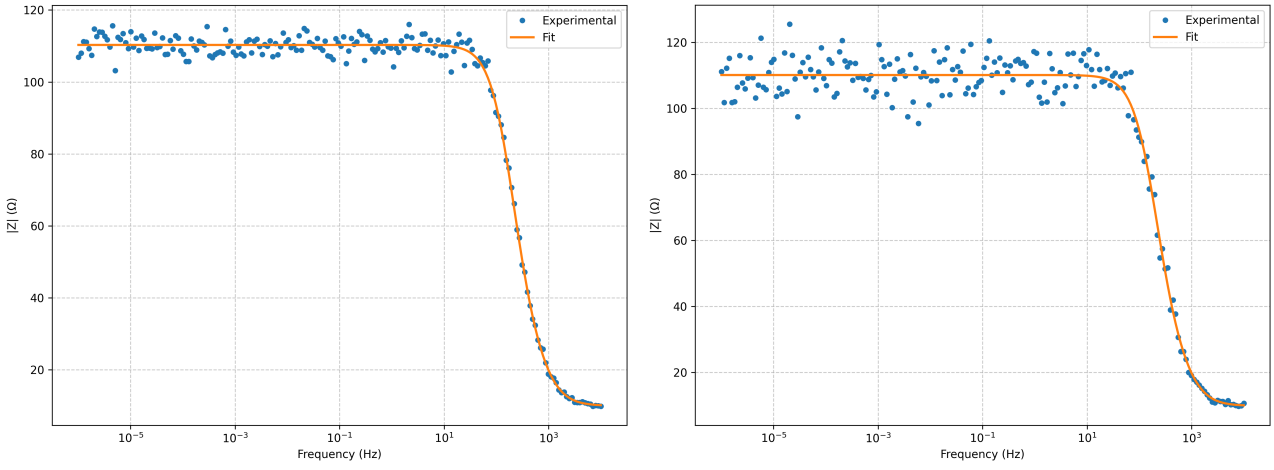
sampling, while the fit reproduces the experimental trace with high fidelity over several decades of frequency. Figures 6–10 present paired subpanels (a: 2.5%; b: 5.0%) for the Nyquist diagram, Bode plots (magnitude and phase), complex residuals, and the Kramers–Kronig validation.

In the Nyquist plots (Figure 6a,b), a well-defined semicircle is observed, with a diameter corresponding to R_{ct}. Increasing noise produces only a larger scatter in the high-frequency region, without altering the global morphology. In the Bode plots (Figures 7 and 8), the phase minimum near $\omega_{\max} \approx 1/(R_{ct}C_{dl})$ is accurately captured for both noise levels. The residuals (Figure 9a,b) remain centered and trend-free; at 5.0% noise, the variance increases without introducing systematic bias. The Kramers–Kronig check (Figure 10) confirms causality and linearity across the full frequency domain.



(**a**) 2.5% noise (**b**) 5.0% noise

Figure 6. Nyquist diagrams for the classic Randles model: (**a**) 2.5% noise; (**b**) 5.0% noise.



(**a**) 2.5% noise (**b**) 5.0% noise

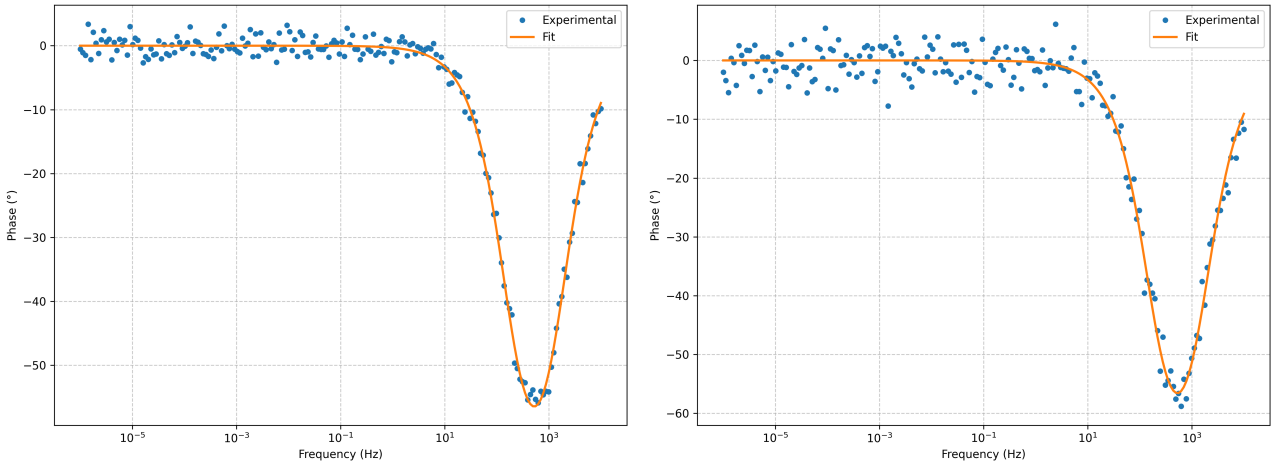
Figure 7. Bode magnitude for the classic Randles model at 2.5% and 5.0% noise levels.

Quantitatively (Table 2), RMSE increases moderately from 3.2200 at 2.5% noise to 6.5700 at 5.0%, while $R^2 \geq 0.971$ and $R^2_{\text{adj}} \geq 0.971$ are maintained in all cases. The estimated parameters fall within the 95% confidence intervals around their nominal values, confirming robust identifiability even under moderate noise.

Table 2. Summary of metrics and parameters for classic Randles ($R_s + (R_{ct} \parallel C_{dl})$). Best fit per noise level.

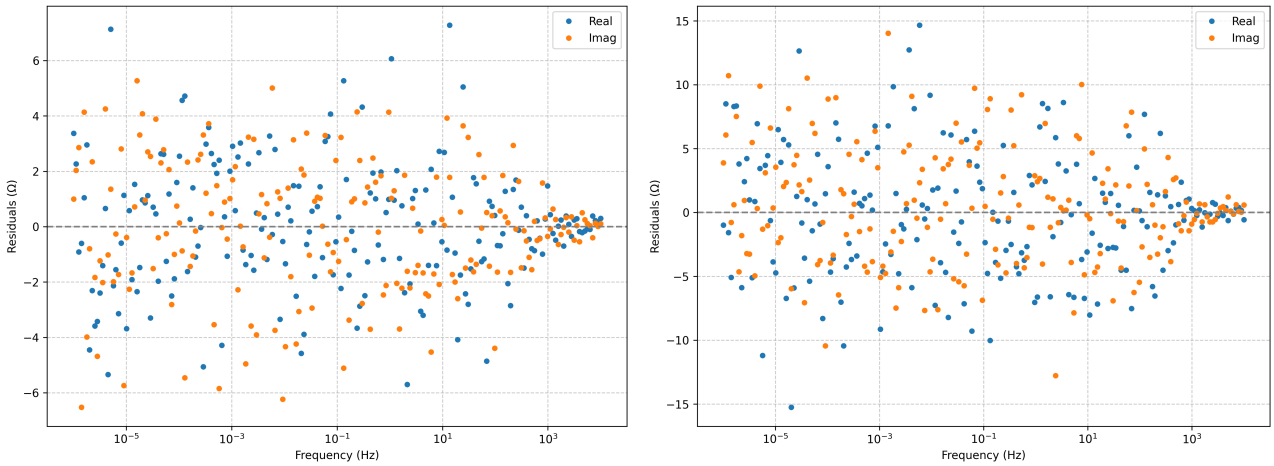
	2.5%	**5.0%**
RMSE	3.2200	6.5700
$\boldsymbol{\chi^2}$	3.5600×10^2	3.4700×10^2
$\boldsymbol{R^2}$	0.9929	0.9709
$\boldsymbol{R^2_{adj}}$	0.9928	0.9707
AIC	362	353
BIC	374	365
Cond#	2.5600×10^{17}	2.3000×10^{17}
R_s [Ω]	10.013 [9.86, 10.14]	9.918 [9.74, 10.14]
R_{ct} [Ω]	100.287 [100.00, 100.67]	100.182 [100.00, 101.11]
C_{dl} [µF]	10.047 [9.991, 10.122]	10.013 [9.994, 10.294]

Values in brackets: 95% confidence intervals. For readability, C_{dl} is reported in µF. Bold entries (RMSE, AIC, BIC, Cond#, and circuit parameters) indicate the key fitting metrics and estimated model parameters highlighted in the discussion.



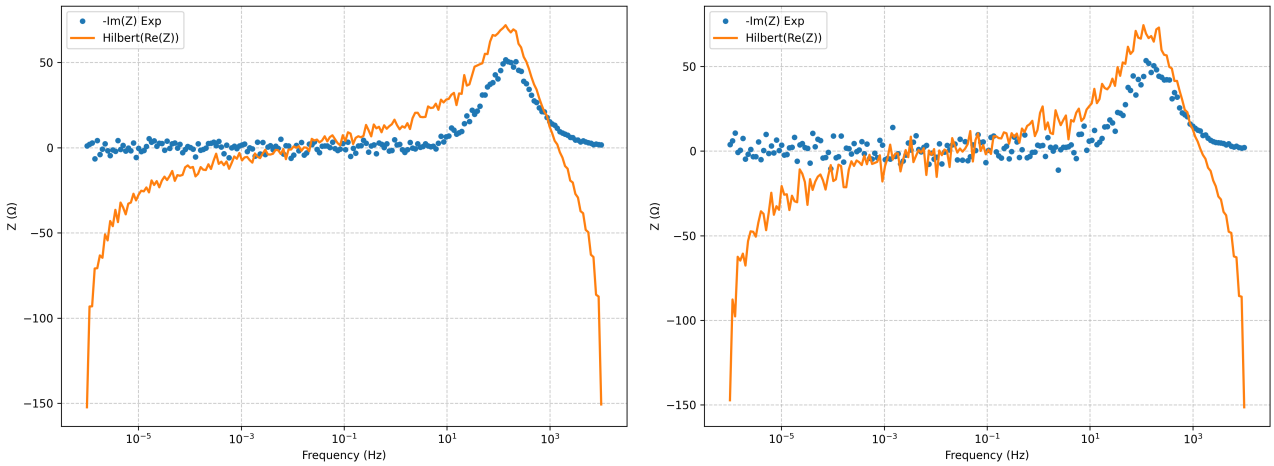
(**a**) 2.5% noise (**b**) 5.0% noise

Figure 8. Bode phase for the classic Randles model at 2.5% and 5.0% noise levels.



(**a**) 2.5% noise (**b**) 5.0% noise

Figure 9. Residuals (real and imaginary parts) for the classic Randles model.



(**a**) 2.5% noise (**b**) 5.0% noise

Figure 10. Kramers–Kronig validation (Hilbert transform) for the classic Randles model.

Overall, these results support the robustness of the classic Randles model for systems dominated by charge-transfer processes and an ideal double-layer capacitance, preserving predictive accuracy and physical consistency under controlled experimental perturbations.

4.2. Model: Randles + CPE $R_s + \left(R_{ct} \parallel \frac{1}{Q(j\omega)^n}\right)$

Increasing the noise level from 2.5% to 5.0% produces a controlled growth in error (RMSE: 3.3100 → 6.5200) and a moderate decrease in R^2 (0.9903 → 0.9634), while preserving spectral agreement (Table 3). The Nyquist diagram retains the characteristic depressed semicircle associated with the CPE (Figure 11), …whereas in the Bode plots (Figures 12a,b and 13a,b) the fit accurately reproduces the magnitude across several decades and precisely locates the phase minimum.

Complex residuals (Figure 14a,b) remain centered and drift-free for both noise levels; the increase in variance at 5.0% is consistent with the added perturbation. The Kramers–Kronig validation (Figure 15a,b) confirms causality and linearity, with no evidence of nonlinearity or nonstationarity.

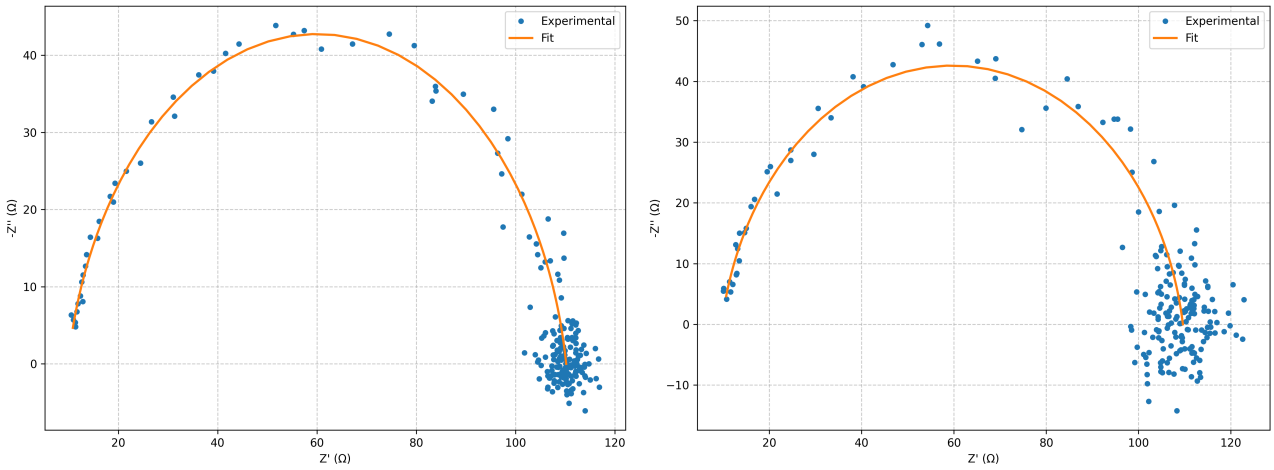
Regarding parameters, R_{ct} remains stable and within its 95% confidence intervals (Table 3), while Q and n exhibit the typical collinearity of non-ideal elements (Cond# $\sim 10^{17}$–10^{18}). For physical interpretation, the effective capacitance is computed using the Brug correction:

$$C_{\text{eff}} = \left[Q\left(R_s^{-1} + R_{ct}^{-1}\right)^{(1-n)}\right]^{1/n},$$

yielding $C_{\text{eff}} \sim$ 2–3 µF for $Q \approx 10\ \mu\text{F s}^{n-1}$, $n \approx 0.90$, $R_s \approx 10\ \Omega$, and $R_{ct} \approx 100\ \Omega$. This corresponds to $\tau \sim 2\text{–}3 \times 10^{-4}$ s and $f_c \sim 10^2$–10^3 Hz, in excellent agreement with the experimentally observed phase minimum.

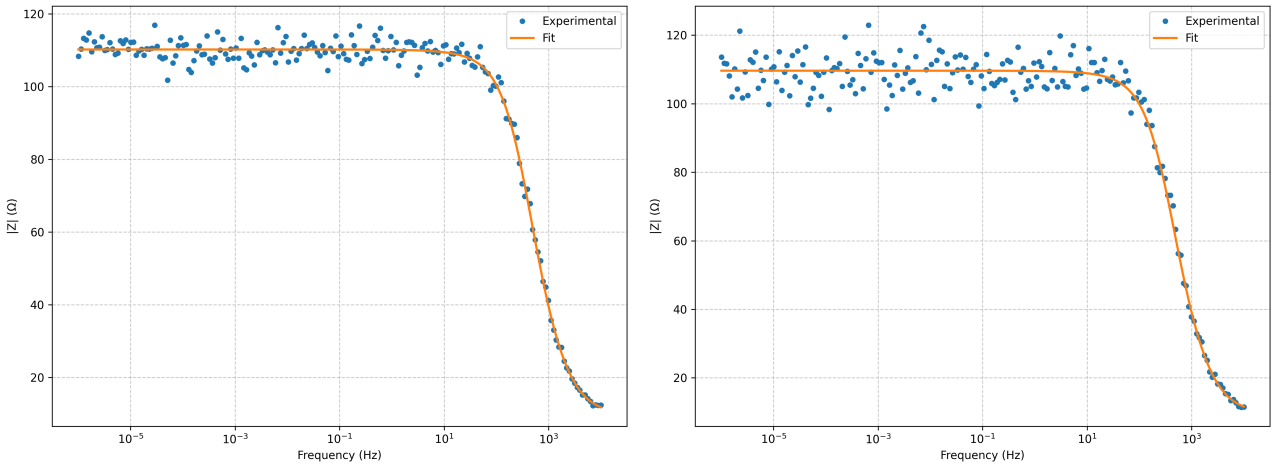
When compared at the same noise level, the classic Randles model is more parsimonious at 2.5% (lower AIC in Table 2; $\Delta\text{AIC} \approx +8$ relative to CPE), whereas at 5.0% Randles+CPE offers a significant advantage (AIC lower in Table 3; $\Delta\text{AIC} \approx -19$), capturing non-idealities without overfitting and preserving white residuals.

In summary, Randles+CPE reproduces with high fidelity the depressed arc and fractional phase shift typical of non-ideal interfaces, outperforming the classic Randles model under conditions of pronounced non-ideality or higher noise, while preserving R_{ct} stability under rigorous statistical and physico-mathematical validation (Figures 11–15; Table 3).



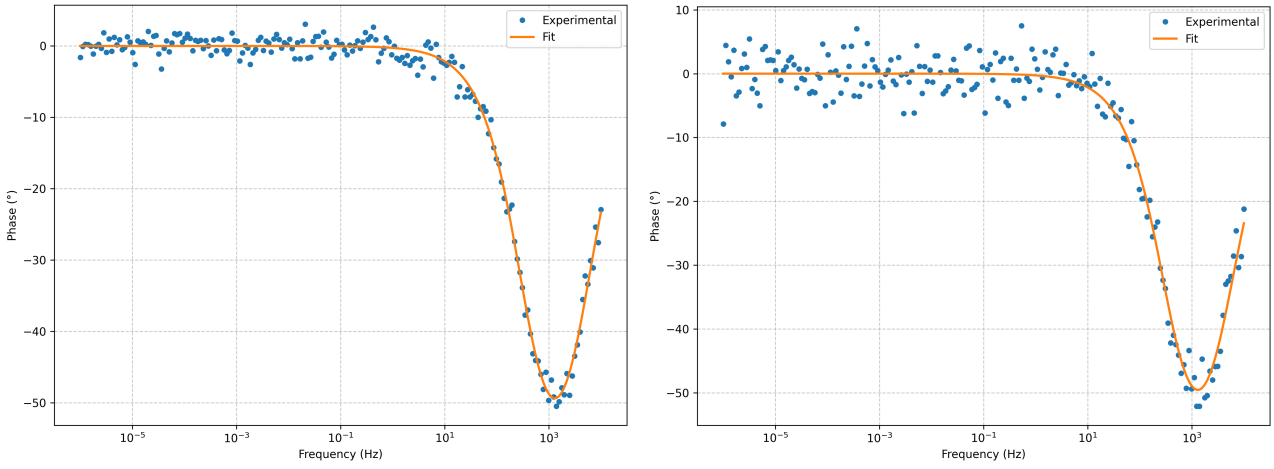
(**a**) 2.5% (**b**) 5.0%

Figure 11. Nyquist diagrams for the Randles+CPE model: comparison between 2.5% and 5.0% noise levels.



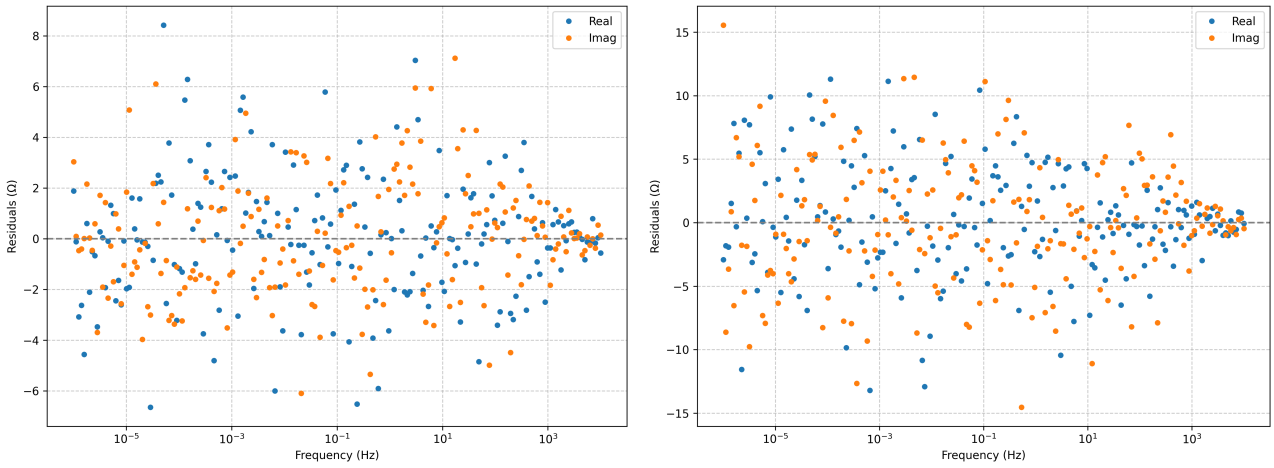
(**a**) 2.5% (**b**) 5.0%

Figure 12. Bode magnitude for the Randles+CPE model: (**a**) 2.5% noise; (**b**) 5.0% noise.



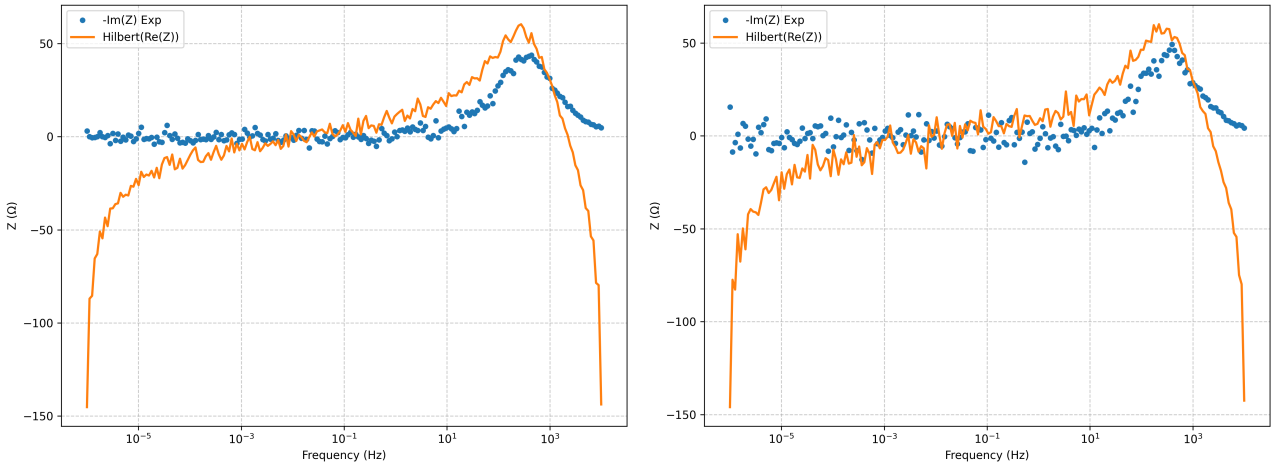
(**a**) 2.5% (**b**) 5.0%

Figure 13. Bode phase for the Randles+CPE model at 2.5% and 5.0% noise levels.



(**a**) 2.5% (**b**) 5.0%

Figure 14. Complex residuals (real and imaginary parts) for the Randles+CPE model.



(**a**) 2.5% (**b**) 5.0%

Figure 15. Kramers–Kronig validation (Hilbert transform) for the Randles+CPE model.

Table 3. Summary of metrics and parameters for Randles + CPE ($R_s + (R_{ct} \parallel \text{CPE})$). Best fit at each noise level.

	2.5%	**5.0%**
RMSE	3.3100	6.5200
$\boldsymbol{\chi^2}$	3.6200×10^2	3.2600×10^2
$\boldsymbol{R^2}$	0.9903	0.9634
$\boldsymbol{R^2_{adj}}$	0.9902	0.9630
AIC	370	334
BIC	386	350
Cond#	1.6700×10^{18}	2.4100×10^{17}
$\boldsymbol{R_s}$ [Ω]	9.862 [9.78, 10.25]	9.688 [9.38, 10.17]
$\boldsymbol{R_{ct}}$ [Ω]	100.353 [100.00, 100.54]	99.935 [99.70, 100.01]
$\boldsymbol{Q}$ [μF s^{n-1}]	10.154 [9.351, 10.339]	10.217 [8.436, 10.549]
$\boldsymbol{n}$ [–]	0.898 [0.90, 0.91]	0.899 [0.89, 0.92]

Values in brackets: 95% confidence intervals. n is dimensionless and Q is reported in μFs^{n-1}. Bold entries (RMSE, AIC, BIC, Cond#, and circuit parameters) indicate the key fitting metrics and estimated model parameters highlighted in the discussion.

4.3. Model: Randles + Warburg $R_s + (R_{ct} \parallel C_{dl}) + \sigma\,\omega^{-1/2}(1-j)$

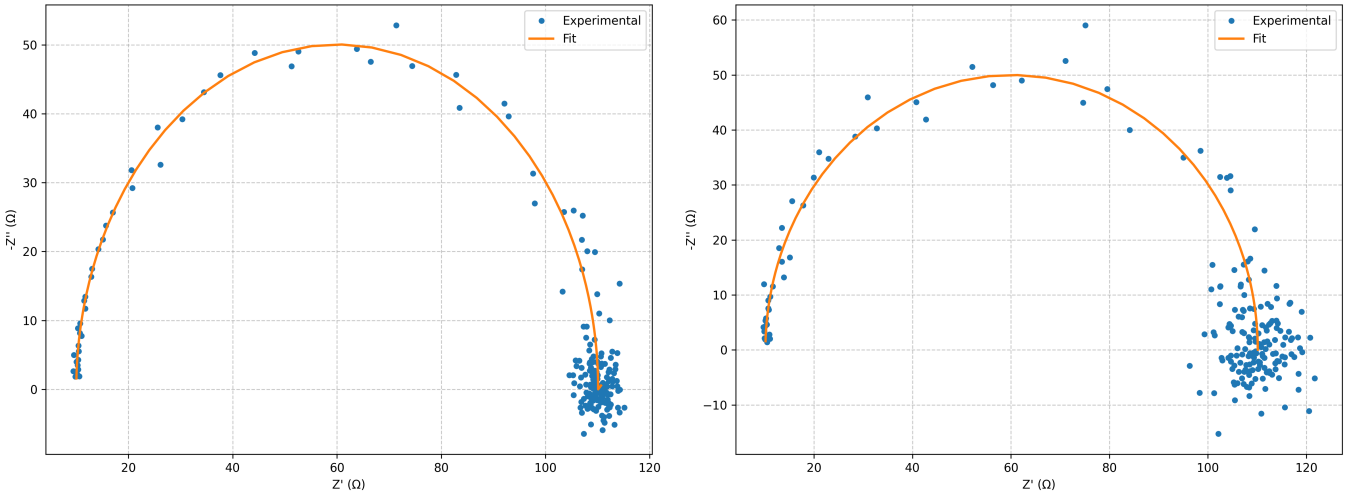
The inclusion of the Warburg element introduces a $4.5000 \times 10^{1}{}^{\circ}$ tail in the (Nyquist plot (Figure 16a,b) and a $-1/2$ slope in the logarithmic magnitude of the Bode plot, accompanied by a phase tending toward -45° at low frequencies (Figures 17a,b and 18a,b). Both features are consistently observed at 2.5% and 5.0% noise levels, supporting the presence of a mass-transport-limiting process.

Increasing the noise level raises the RMSE from 3.1900 to 6.3800 and reduces R^2 from 0.9930 to 0.9725 (Table 4), while maintaining close agreement in both Nyquist and Bode domains (Figures 16–18). Residuals remain centered and trend-free (Figure 19a,b), and Kramers–Kronig validation confirms causality and linearity (Figure 20a,b), ruling out artifacts from nonlinearity or nonstationarity.

R_s, R_{ct}, and C_{dl} are estimated stably with narrow 95% confidence intervals at both noise levels (Table 4). In contrast, the effective diffusivity σ_W shows greater uncertainty, especially at 5.0%, where the 95% CI reaches the lower bound of the fit (1.0000×10^{-6}–9.4900×10^{-4}). This indicates that, within the available frequency window, the diffusive component is morphologically detectable (Figures 16 and 18) but its magnitude is partially ill-conditioned. Extending the frequency sweep to lower values and/or using a finite-length Warburg variant (e.g., with τ_D) would help constrain σ_W.

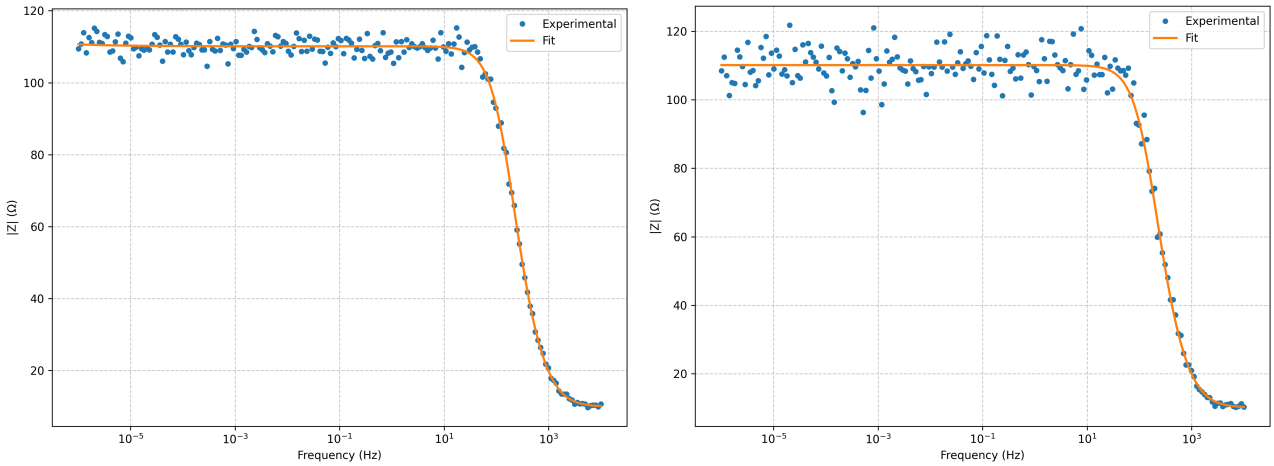
The phase trend toward -45° (Figure 18) and the tail in the Nyquist plot (Figure 16) are consistent with semi-infinite diffusion of electroactive species to/from the interface. The stability of R_{ct} under noise confirms that the faradaic kinetics are well identified, with the main variation residing in the mass-transport component (Table 4).

Compared to the classic Randles model, adding the Warburg element improves model likelihood at both noise levels (AIC: 349 vs. 362 at 2.5% ; 348 vs. 353 at 5.0% ; cf. Table 4 vs. Table 2). This indicates that the diffusive signature adds genuine information without overfitting, consistent with white residuals (Figure 19) and the KK validation (Figure 20).



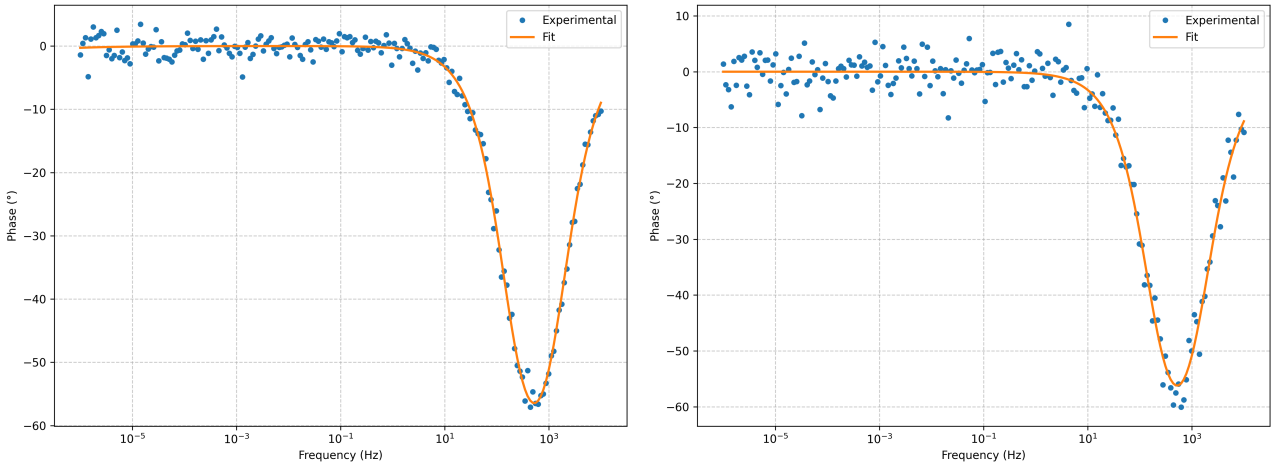
(**a**) 2.5% (**b**) 5.0%

Figure 16. Nyquist diagrams for the Randles+Warburg model: comparison between 2.5% and 5.0% noise levels.



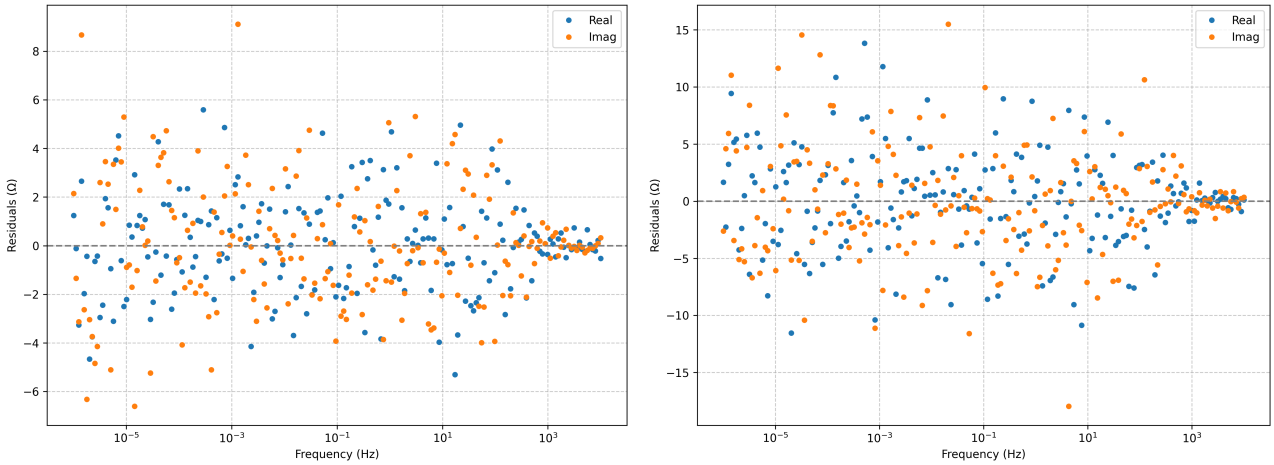
(**a**) 2.5% (**b**) 5.0%

Figure 17. Bode magnitude plots for the Randles+Warburg model at 2.5% and 5.0% noise levels.



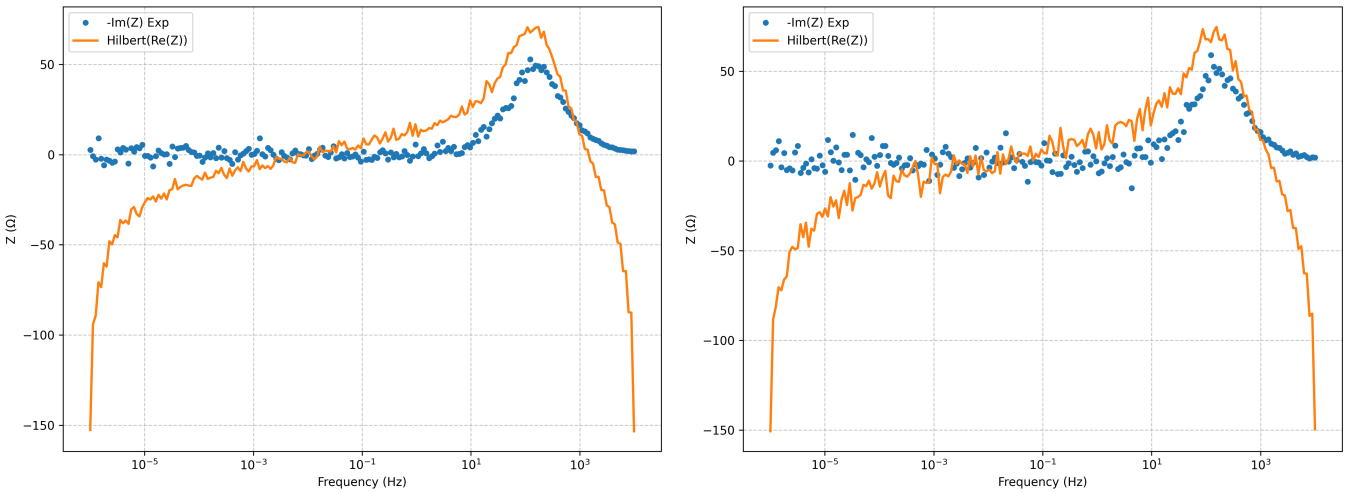
(**a**) 2.5% (**b**) 5.0%

Figure 18. Bode phase plots for the Randles+Warburg model at 2.5% and 5.0% noise levels.



(**a**) 2.5% (**b**) 5.0%

Figure 19. Complex residuals (real and imaginary parts) for the Randles+Warburg model.



(**a**) 2.5% (**b**) 5.0%

Figure 20. Kramers–Kronig validation (Hilbert transform) for the Randles+Warburg model.

Table 4. Summary of metrics and parameters for Randles + Warburg ($R_s + (R_{ct} \parallel C_{dl}) + Z_W$). Best fit at each noise level.

	2.5%	**5.0%**
RMSE	3.1900	6.3800
$\boldsymbol{\chi^2}$	3.4100×10^2	3.4000×10^2
$\boldsymbol{R^2}$	0.9930	0.9725
$\boldsymbol{R^2_{adj}}$	0.9929	0.9723
AIC	349	348
BIC	365	364
Cond#	3.1900×10^{17}	2.7400×10^{17}
$\boldsymbol{R_s}$ [Ω]	9.993 [9.87, 10.13]	10.145 [9.98, 10.34]
$\boldsymbol{R_{ct}}$ [Ω]	100.116 [100.00, 100.54]	99.977 [100.00, 101.18]
$\boldsymbol{C_{dl}}$ [µF]	10.059 [10.000, 10.147]	10.015 [9.999, 10.181]
$\boldsymbol{\sigma_W}$ [$\Omega\,s^{-1/2}$]	1.3800×10^{-3} [1.0000×10^{-6}, 3.5800×10^{-3}]	8.2500×10^{-6} [1.0000×10^{-6}, 9.4900×10^{-4}]

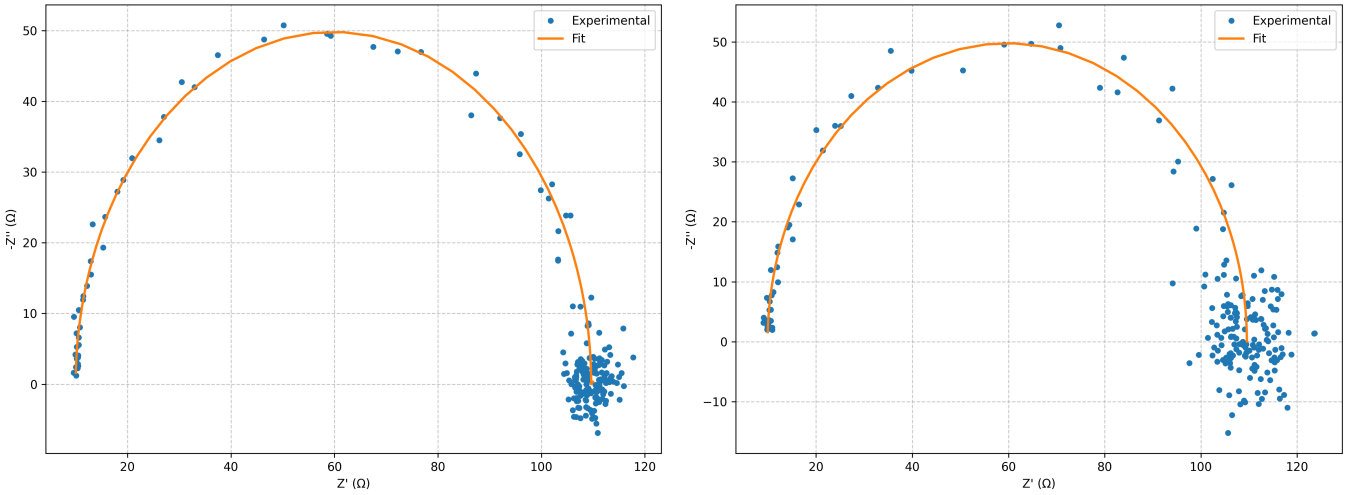
Values in brackets: 95% confidence intervals. σ_W is reported in $\Omega s^{-1/2}$ and defined as $Z_W = \sigma_W(1-j)/\sqrt{\omega}$. Bold entries (RMSE, AIC, BIC, Cond#, and circuit parameters) indicate the key fitting metrics and estimated model parameters highlighted in the discussion.

4.4. Model: $(R_{ct} + Z_W) \parallel C_{dl}$

The series combination $R_{ct} + Z_W$, placed in parallel with C_{dl}, reproduces an arc with a diffusive tail in the Nyquist plot (Figure 21a,b). In the Bode magnitude representation, the fit accurately follows the simulated data over several frequency decades (Figure 22a,b), while the phase exhibits the expected drift toward the diffusion-controlled regime (approaching $-45°$ at low frequencies; Figure 23). Increasing noise from 2.5% to 5.0% barely affects the morphological agreement, with discrepancies mainly concentrated at high frequencies, where the capacitive pathway of C_{dl} dominates.

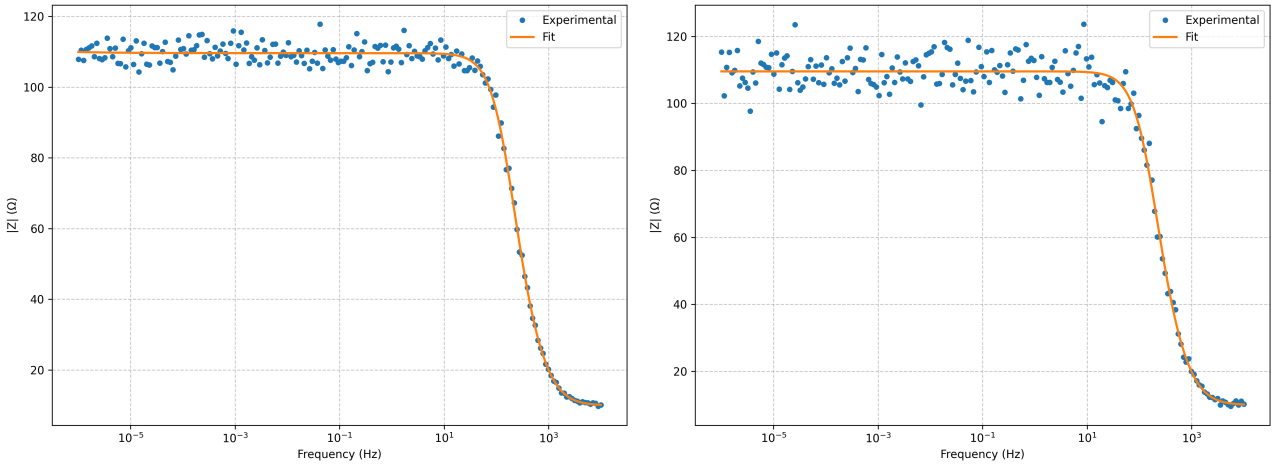
The RMSE increases from 3.3300 to 6.4700, and R^2 decreases from 0.9923 to 0.9717 (Table 5), while maintaining close agreement with the reference spectrum. The residuals (real and imaginary parts) remain centered without any trend (Figure 24a,b), and the Kramers–Kronig (Hilbert transform) validation confirms causality and linearity of the simulated spectrum at both noise levels (Figure 25).

The parameters R_s, R_{ct}, and C_{dl} are stable and have narrow 95% confidence intervals (Table 5). The diffusive amplitude σ_W is the least constrained: at 2.5% noise it exhibits a wide 95% CI $[1.0000 \times 10^{-6}, 3.7600 \times 10^{-3}]$, and at 5.0% it reaches the lower bound of the fit $[1.0000 \times 10^{-6}, 4.6900 \times 10^{-3}]$. This indicates that, within the available frequency window, the diffusive signature is visible (Figures 21 and 23), but its amplitude is partially ill-conditioned due to the capacitive shunt. The condition number is moderate ($\sim 8.0000 \times 10^5$), significantly better than in CPE-based models, supporting the overall numerical stability of the fit.



(**a**) 2.5% noise (**b**) 5.0% noise

Figure 21. Nyquist plots for $(R_{ct} + Z_W) \parallel C_{dl}$: comparison between 2.5% and 5.0% noise levels.



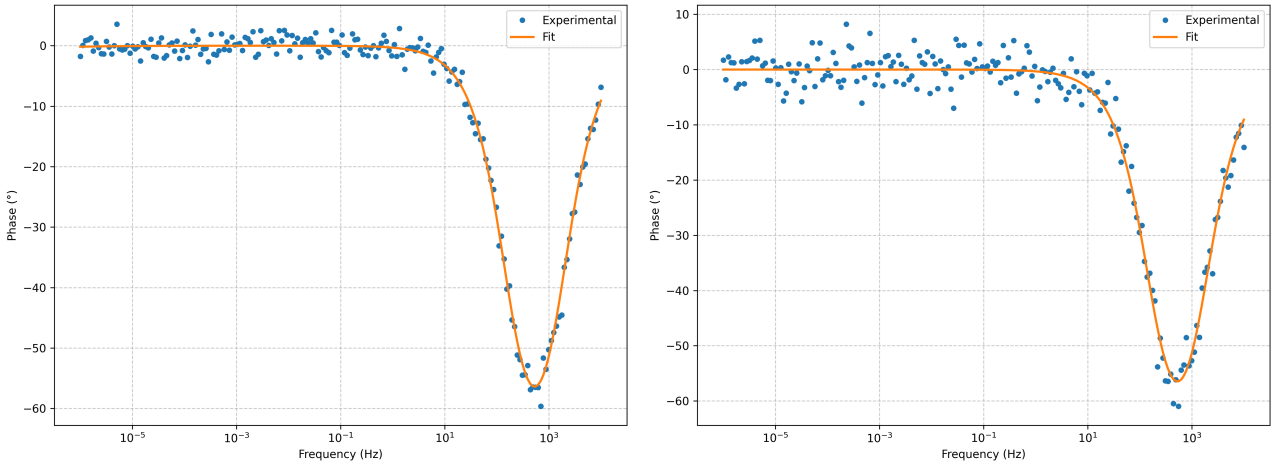
(**a**) 2.5% noise (**b**) 5.0% noise

Figure 22. Bode magnitude plots for $(R_{ct} + Z_W) \parallel C_{dl}$ at 2.5% and 5.0% noise.

The parallel arrangement with C_{dl} shunts the faradaic branch at high frequencies (almost purely capacitive trajectories), while at low frequencies $R_{ct} + Z_W$ dominates, producing the $4.5000 \times 10^{1\circ}$ diffusive tail (Figures 21 and 23). The constancy of R_{ct} under noise suggests that the interfacial kinetics are well-identified, with the main uncertainty arising from the effective mass transport term encapsulated in σ_W.

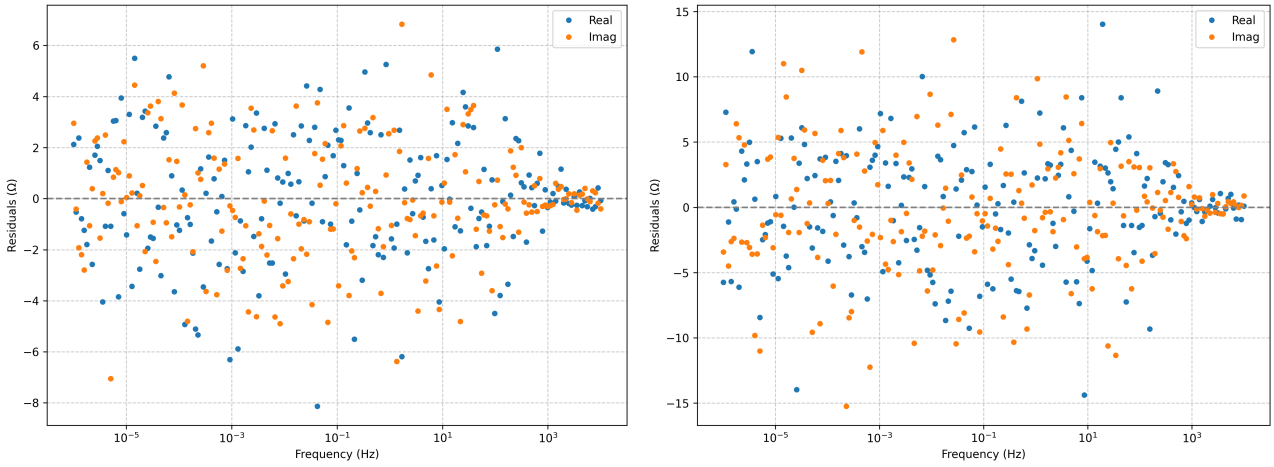
At 2.5% noise, this model is less statistically supported than Randles+Warburg and Randles+CPE (AIC = 382 vs. 349 and 370; ΔAIC = +33 and +12, respectively), and even less than the classical Randles (362; ΔAIC = +20). At 5.0%, its performance approaches that of the classical Randles (354 vs. 353; ΔAIC = +1), but remains below Randles+Warburg (348; ΔAIC = +6) and particularly Randles+CPE (334; ΔAIC = +20). Overall, the statistical evidence favors alternative descriptions when the available frequency window does not sufficiently constrain σ_W.

The $(R_{ct} + Z_W) \parallel C_{dl}$ topology captures the expected kinetic-diffusive interaction and produces physically consistent fits (Figures 21–25); however, under the current measurement window its informational advantage is limited compared to Randles+Warburg or Randles+CPE, due to the poor constraint on σ_W.



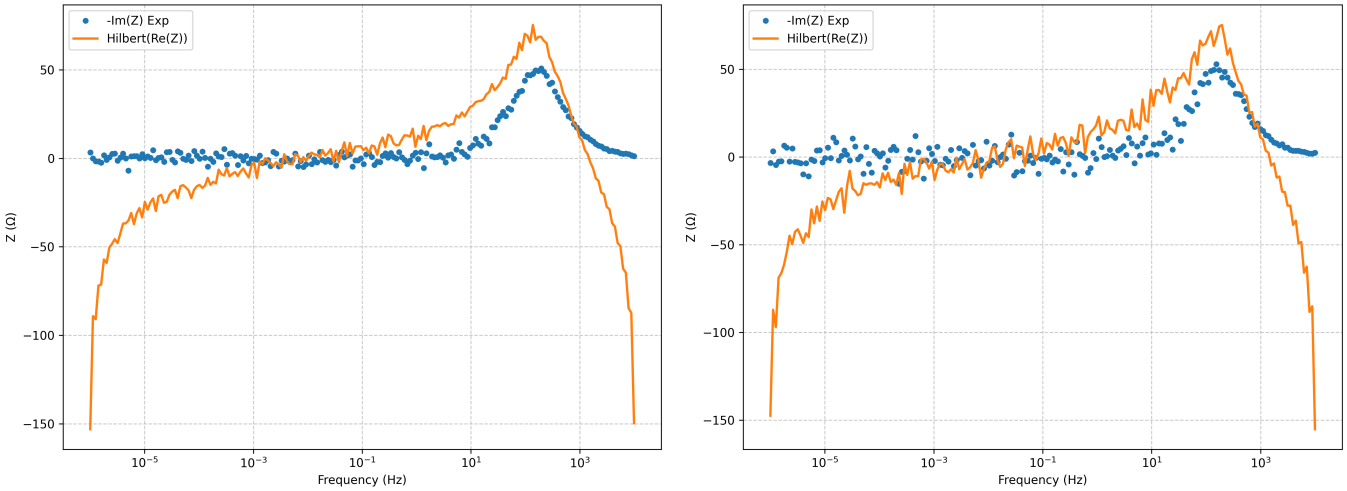
(**a**) 2.5% noise (**b**) 5.0% noise

Figure 23. Bode phase plots for $(R_{ct} + Z_W) \parallel C_{dl}$ at 2.5% and 5.0% noise.



(**a**) 2.5% noise (**b**) 5.0% noise

Figure 24. Residuals (real and imaginary parts) for $(R_{ct} + Z_W) \parallel C_{dl}$.



(**a**) 2.5% noise (**b**) 5.0% noise

Figure 25. Kramers–Kronig validation (Hilbert transform) for $(R_{ct} + Z_W) \parallel C_{dl}$.

Table 5. Summary of metrics and fitted parameters for $(R_{ct} + Z_W) \parallel C_{dl}$ with series resistance R_s. Best fit at each noise level.

	2.5% Noise	**5.0% Noise**
RMSE	3.3300	6.4700
$\boldsymbol{\chi^2}$	3.7400×10^2	3.4600×10^2
$\boldsymbol{R^2}$	0.9923	0.9717
$\boldsymbol{R^2_{adj}}$	0.9922	0.9714
AIC	382	354
BIC	398	370
Cond#	7.9600×10^5	7.9600×10^5
$\boldsymbol{R_s}$ [Ω]	9.995 [9.85, 10.11]	9.936 [9.67, 10.22]
$\boldsymbol{R_{ct}}$ [Ω]	99.625 [99.17, 100.03]	99.625 [98.90, 100.30]
$\boldsymbol{\sigma_W}$ [$\Omega\,s^{-1/2}$]	8.4700×10^{-4} [1.0000×10^{-6}, 3.7600×10^{-3}]	1.0000×10^{-6} [1.0000×10^{-6}, 4.6900×10^{-3}]
$\boldsymbol{C_{dl}}$ [µF]	9.909 [9.801, 10.016]	10.002 [9.711, 10.235]

Values in brackets: 95% confidence intervals. σ_W is reported in $\Omega s^{-1/2}$ and defined as $Z_W = \sigma_W(1-j)/\sqrt{\omega}$. C_{dl} is reported in µF for clarity. Bold entries (RMSE, AIC, BIC, Cond#, and circuit parameters) indicate the key fitting metrics and estimated model parameters highlighted in the discussion.

4.5. Model: $(R_{ct} + Z_W) \parallel$ CPE

This topology combines semi-infinite diffusion (Z_W) with a non-ideal capacitive response (CPE). In the Nyquist plot, a depressed arc appears along with a diffusive extension at low frequencies (Figure 26a,b); in the Bode magnitude plot, the fit reproduces the spectrum across several decades (Figure 27a,b) and captures the fractional phase minimum associated with $n < 1$ (Figure 28a,b).

Increasing the noise from 2.5% to 5.0% raises the RMSE from 3.2900 to 6.4400 and reduces R^2 from 0.9904 to 0.9645 (Table 6), while preserving morphological agreement in both representations. The residuals remain centered and trend-free (Figure 29a,b); the Kramers–Kronig test confirms causality and linearity of the spectrum (Figure 30a,b).

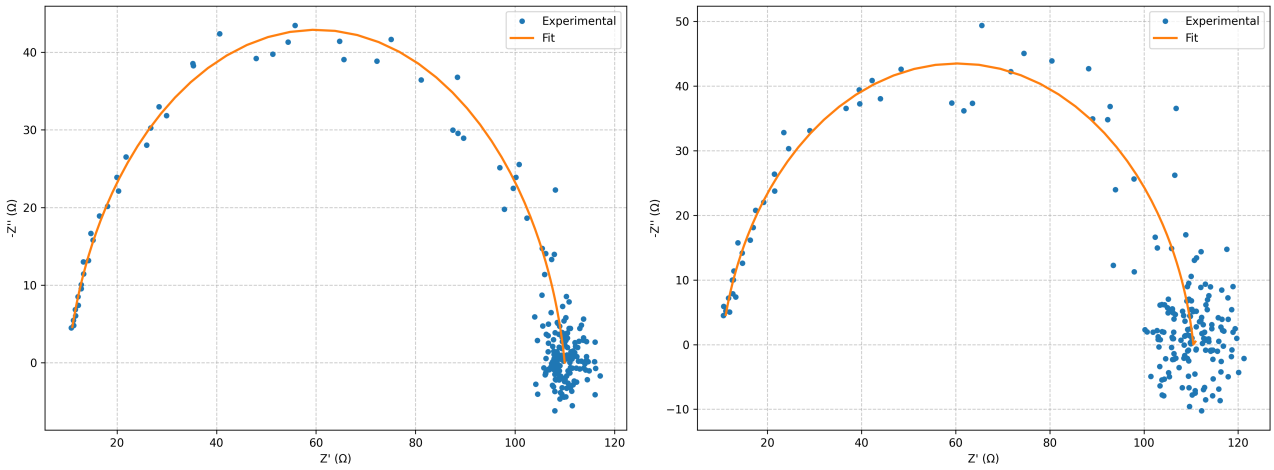
The parameters R_s and R_{ct} are stable with narrow 95% confidence intervals at both noise levels (Table 6). The exponent $n \approx 0.90$ indicates a distribution of relaxation times consistent with interfacial heterogeneity/roughness; $Q \sim$ 9–10 µF s^{n-1} corresponds to an effective capacitance of $\sim$2–3 µF (using Brug's correction, as in the CPE subsection). The diffusive amplitude σ_W is the least constrained at 2.5% noise (95% CI reaches the

lower bound), but is better defined at 5.0%. The condition number is moderate (Cond# $\sim 2.2 \times 10^6$), much lower than for models with CPE only, suggesting reduced collinearity between (Q, n) and the diffusive branch when Z_W is present.

The CPE accounts for interfacial non-idealities (distribution of time constants), while Z_W captures mass-transport control at low frequencies. The phase transition toward $-45°$ (Figure 28) and the Nyquist tail (Figure 26) highlight the diffusive contribution; the stability of R_{ct} supports a well-identified faradaic kinetics.

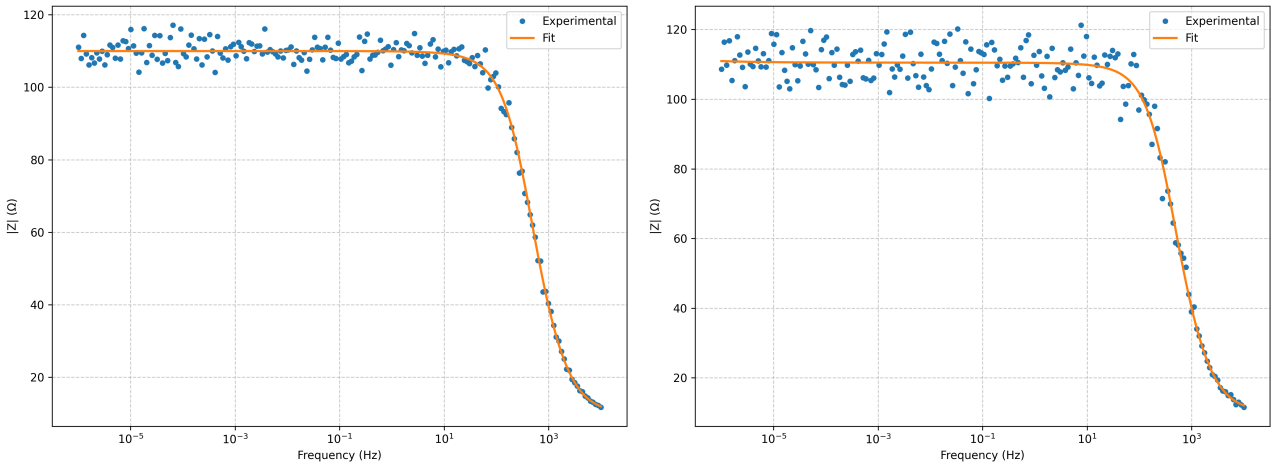
At 2.5% noise, this model markedly outperforms the classical Randles (AIC 352 vs. 362; ΔAIC = -10) and Randles+CPE (352 vs. 370; -18), and is close to Randles+Warburg (352 vs. 349; $+3$). At 5.0%, it becomes the best-performing alternative among those considered (AIC 333), surpassing Randles+CPE (334), Randles+Warburg (348), and the classical Randles (353) (Table 6 and related tables). This suggests that when interfacial non-ideality and a diffusive component are present simultaneously, the $(R_{ct} + Z_W) \parallel$ CPE architecture offers the best balance between fit quality and parsimony.

The combination of CPE and Warburg in parallel with R_{ct} provides a coherent and statistically preferred representation of systems exhibiting concurrent interfacial non-ideality and diffusion, with white residuals and consistent KK validation (Figures 26–30; Table 6).



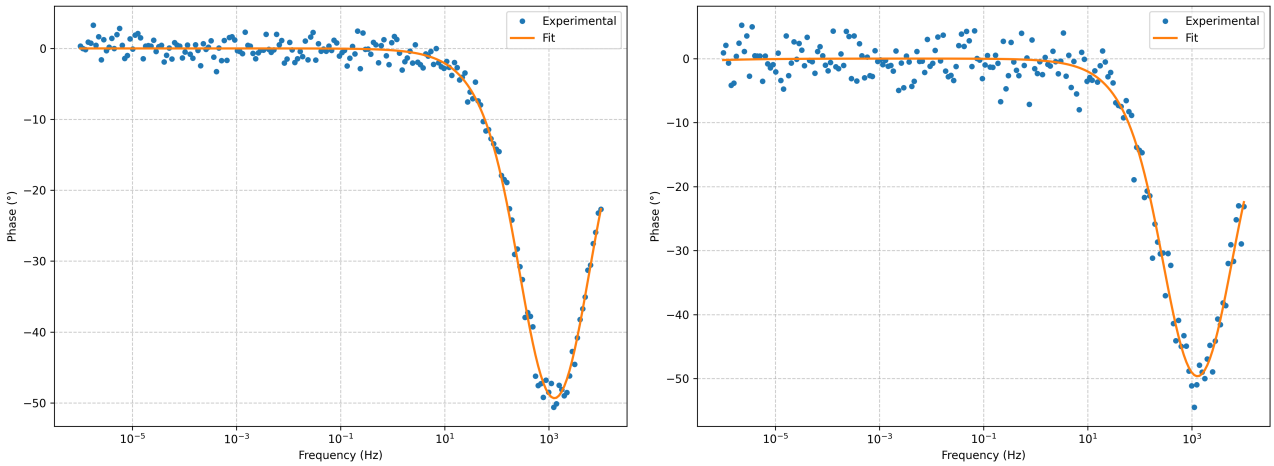
(**a**) 2.5% noise (**b**) 5.0% noise

Figure 26. Nyquist plots for $(R_{ct} + Z_W) \parallel$ CPE: comparison between 2.5% and 5.0% noise levels.



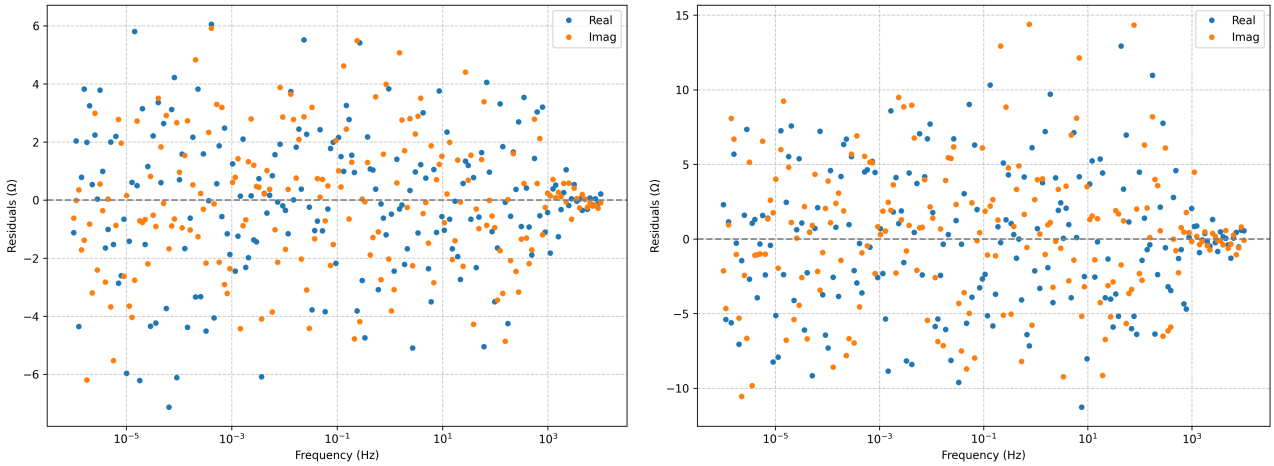
(**a**) 2.5% noise (**b**) 5.0% noise

Figure 27. Bode magnitude plots for $(R_{ct} + Z_W) \parallel$ CPE at 2.5% and 5.0% noise.



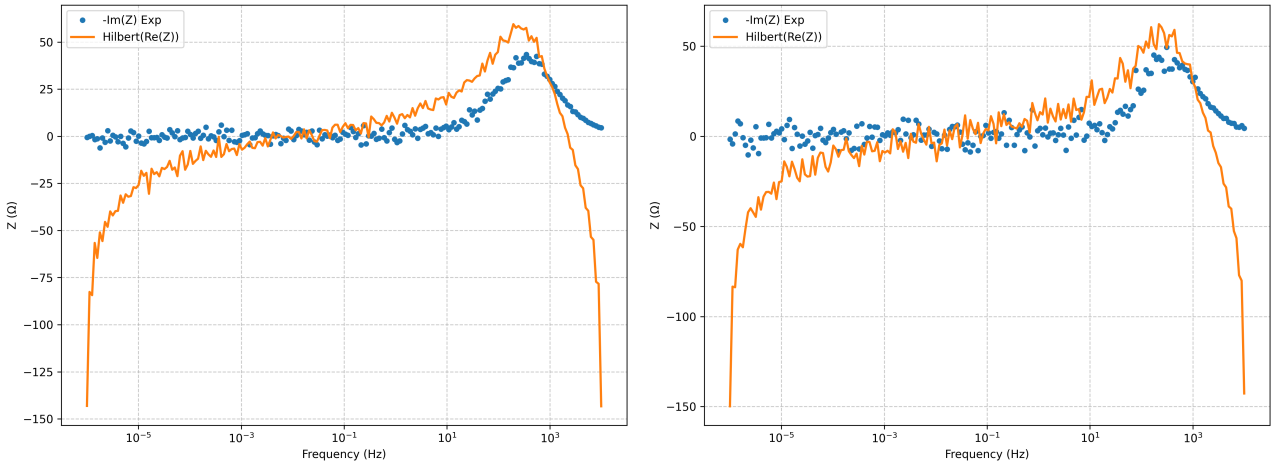
(**a**) 2.5% noise (**b**) 5.0% noise

Figure 28. Bode phase plots for $(R_{ct} + Z_W) \parallel$ CPE at 2.5% and 5.0% noise.



(**a**) 2.5% noise (**b**) 5.0% noise

Figure 29. Residuals (real and imaginary parts) for $(R_{ct} + Z_W) \parallel$ CPE.



(**a**) 2.5% noise (**b**) 5.0% noise

Figure 30. Kramers–Kronig validation (Hilbert transform) for $(R_{ct} + Z_W) \parallel$ CPE.

Table 6. Summary of metrics and parameters for $(R_{ct} + Z_W) \parallel$ CPE with series resistance R_s. Best fit at each noise level.

	2.5% Noise	**5.0% Noise**
RMSE	3.2900	6.4400
$\boldsymbol{\chi^2}$	3.4200×10^2	3.2300×10^2
$\boldsymbol{R^2}$	0.9904	0.9645
$\boldsymbol{R^2_{adj}}$	0.9903	0.9641
AIC	352	333
BIC	372	353
Cond#	2.2000×10^6	2.2300×10^6
$\boldsymbol{R_s}$ [Ω]	10.103 [9.91, 10.29]	10.274 [9.78, 10.78]
$\boldsymbol{R_{ct}}$ [Ω]	99.866 [99.36, 100.28]	100.221 [99.07, 101.11]
$\boldsymbol{\sigma_W}$ [$\Omega\,s^{-1/2}$]	1.0000×10^{-6} [1.0000×10^{-6}, 4.8800×10^{-4}]	1.1400×10^{-3} [1.0000×10^{-6}, 6.0100×10^{-3}]
$\boldsymbol{Q}$ [$\mu F\,s^{n-1}$]	9.762 [9.151, 10.434]	9.092 [7.652, 10.340]
$\boldsymbol{n}$ [–]	0.904 [0.90, 0.91]	0.910 [0.90, 0.93]

Values in brackets: 95% confidence intervals. σ_W is reported in $\Omega s^{-1/2}$; Q is reported in $\mu F s^{n-1}$; n is dimensionless. Bold entries (RMSE, AIC, BIC, Cond#, and circuit parameters) indicate the key fitting metrics and estimated model parameters highlighted in the discussion.

4.6. Model: Full Randles

The model reliably reproduces the canonical features: a depressed semicircle at intermediate frequencies and a diffusive tail at low frequencies (Nyquist, Figure 31a,b). The Bode magnitude and phase plots (Figures 32a,b and 33a,b) show a consistent magnitude decay around the characteristic frequency and a fractional phase minimum due to the CPE contribution.

When increasing noise from 2.5% to 5.0%, the *RMSE* rises from 3.2700 to 6.6200 and R^2 decreases from 0.9905 to 0.9625 (Table 7), but the overall morphology of both Nyquist and Bode representations remains preserved.

Ohmic and kinetic parameters remain stable (narrow 95% CIs in R_s and R_{ct}; Table 7). In contrast, Q, n, and particularly the effective diffusivity σ exhibit marked collinearity (Cond# $\sim 10^{11}$), with σ reaching the upper bound of its interval at 2.5%. This indicates that, within the available frequency range, the CPE–Warburg separation is not fully resolved: the CPE absorbs part of the diffusive curvature and vice versa. A practical way to express the capacitive response is to report, along with Q and n, the effective capacitance C_{eff} (Brug correction), which is on the order of a few µF, consistent with the position of the phase minimum (Figure 33).

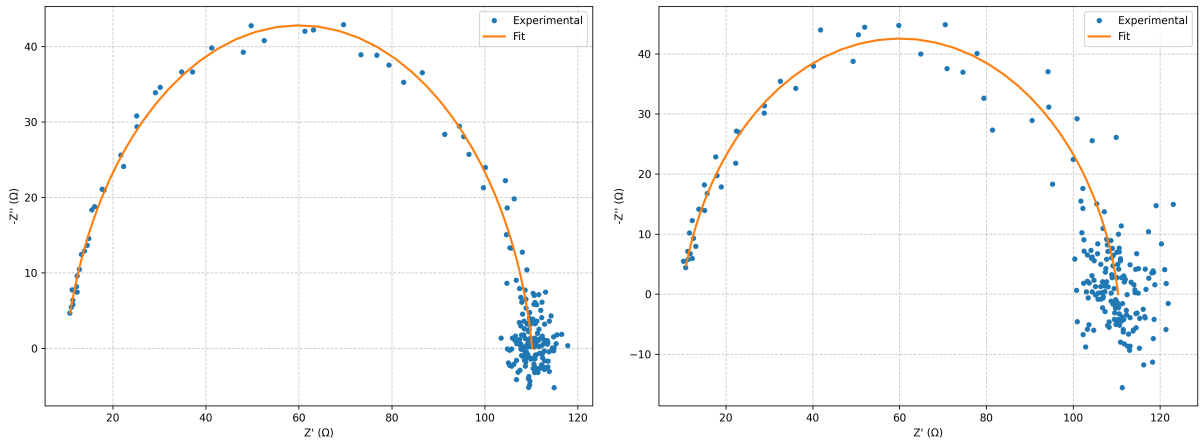
The residuals (Figure 34a,b) remain centered and free from systematic trends; only their variance increases in proportion to the noise level, confirming statistical robustness. The Kramers–Kronig validation (Figure 35a,b) further confirms the internal consistency, causality, and linearity of the fitted spectra, with bounded deviations at the spectral limits due to the finite frequency window.

The exponent $n \approx 0.90$ reflects a distribution of relaxation times related to interfacial roughness and heterogeneity, while the -45° tail and slope corroborate the presence of a mass-transport component (Warburg). The stability of $R_{ct} \approx 100\ \Omega$ at both noise levels confirms well-defined faradaic kinetics, decoupled from the uncertainties in Q, n, and σ (Table 7).

At 2.5%, the *AIC* of the full Randles (350) is comparable to Randles+Warburg (349) and better than Randles+CPE (370), but it does not provide a material advantage over the simpler variants (Figures 31–33; Table 7). At 5.0%, the model is penalized for complexity (AIC 356; BIC 376) compared to more parsimonious alternatives, especially $(R_{ct} + Z_W) \parallel$

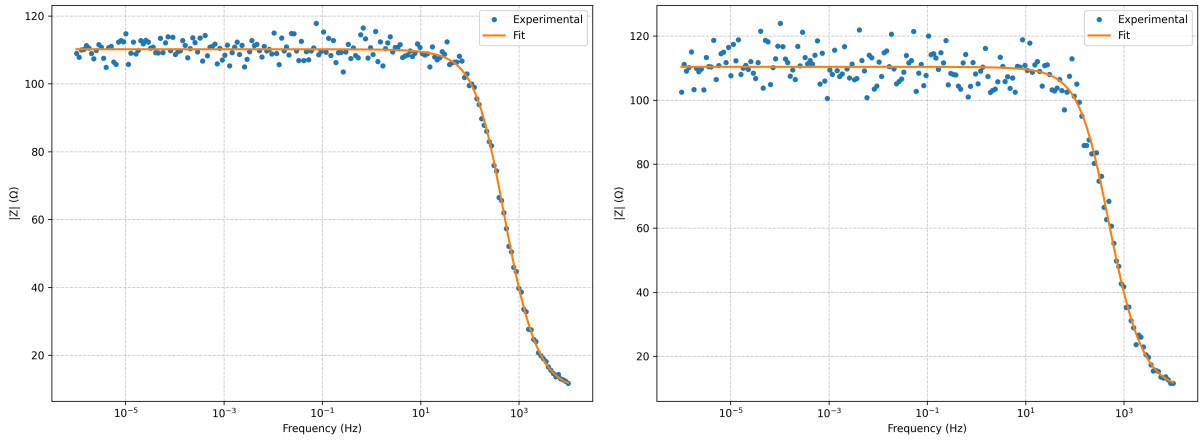
CPE and Randles+CPE, which achieve lower AIC values with equal or better fidelity. Consequently, if σ is poorly bounded and the AIC improvement is marginal, the full version is not statistically justified.

The full Randles model simultaneously captures interfacial non-ideality and diffusion, but within the present spectral range, the gain over partial models is limited and the identifiability of σ remains fragile. For data with mild non-ideality and moderate diffusion, $(R_{ct} + Z_W) \parallel$ CPE or Randles+Warburg offer a superior trade-off between physical realism and parsimony; the full model should be reserved for spectra with clear and quantifiable evidence of both contributions (Figures 31–35; Table 7).



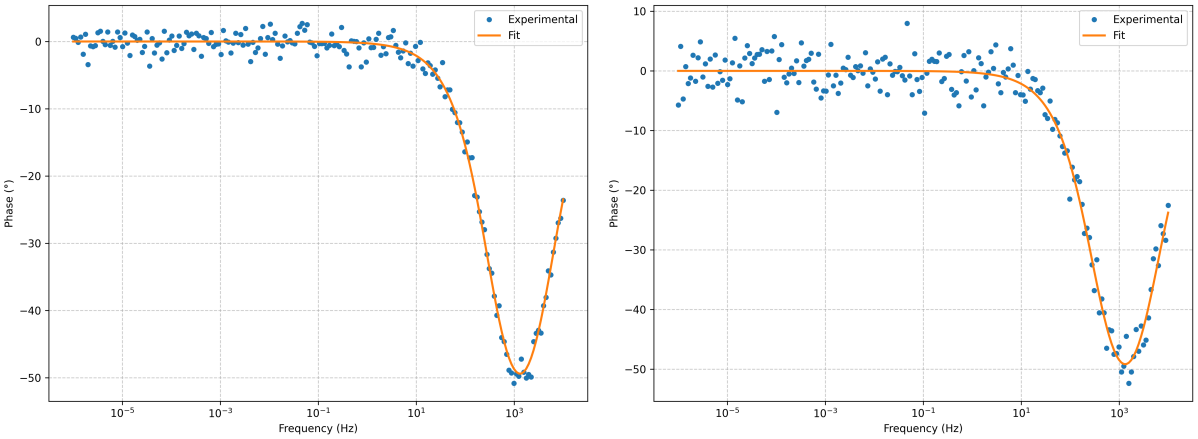
(**a**) 2.5% noise (**b**) 5.0% noise

Figure 31. Nyquist plots for the full Randles model: comparison between 2.5% and 5.0% noise.



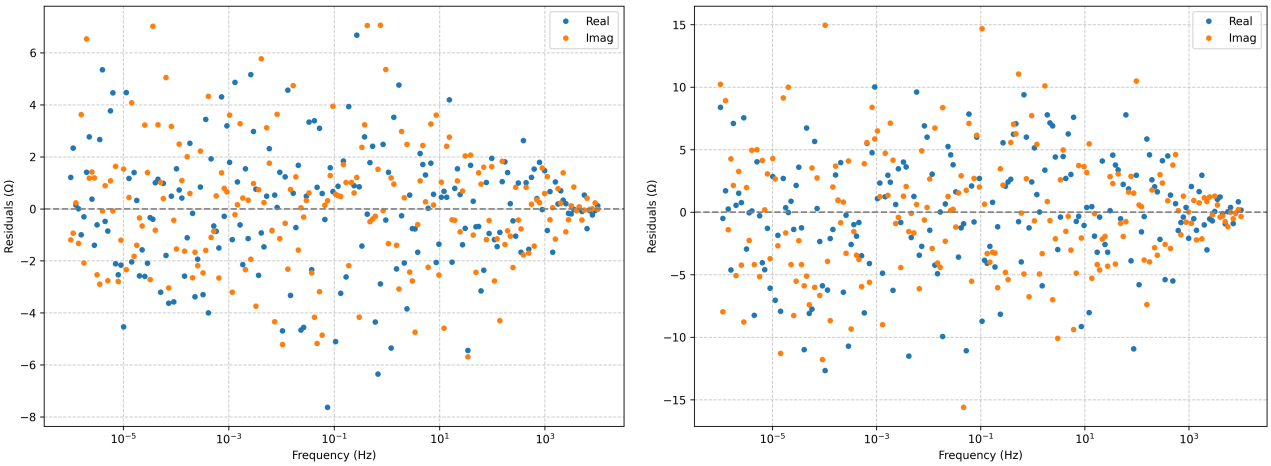
(**a**) 2.5% noise (**b**) 5.0% noise

Figure 32. Bode magnitude for the full Randles model at 2.5% and 5.0% noise.



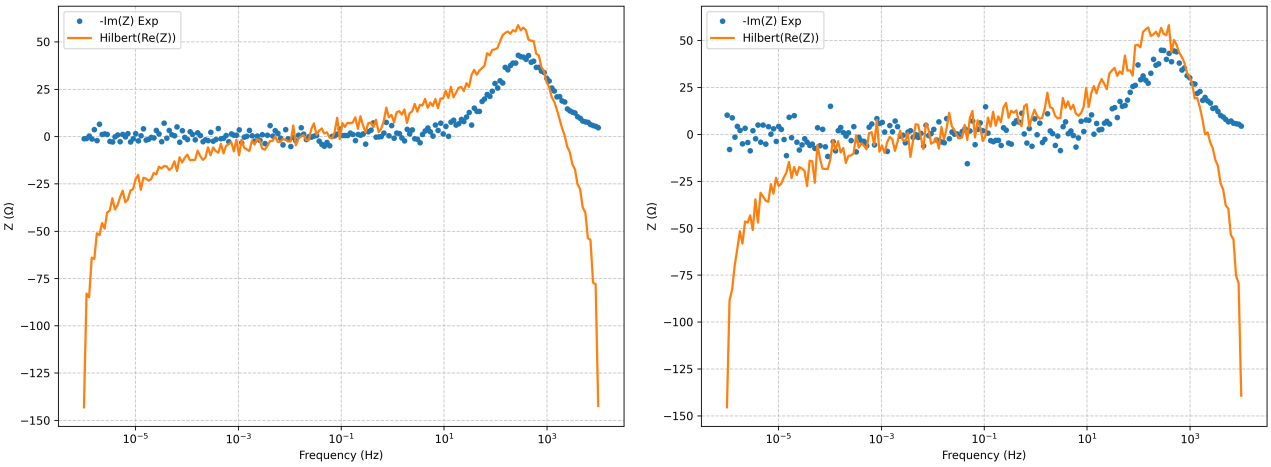
(**a**) 2.5% noise (**b**) 5.0% noise

Figure 33. Bode phase for the full Randles model at 2.5% and 5.0% noise.



(**a**) 2.5% noise (**b**) 5.0% noise

Figure 34. Residuals (real and imaginary parts) for the full Randles model.



(**a**) 2.5% noise (**b**) 5.0% noise

Figure 35. Kramers–Kronig (Hilbert transform) validation for the full Randles model.

Table 7. Summary of metrics and parameters for full Randles: $R_s + \left(R_{ct} \parallel \left(\frac{1}{Q(j\omega)^n} + \frac{\sigma(1-j)}{\sqrt{\omega}}\right)\right)$. Best fit for each noise level.

	2.5%	**5.0%**
RMSE	3.2700	6.6200
$\boldsymbol{\chi^2}$	3.4000×10^2	3.4600×10^2
$\boldsymbol{R^2}$	0.9905	0.9625
$\boldsymbol{R^2_{adj}}$	0.9904	0.9620
AIC	350	356
BIC	369	376
Cond#	1.4000×10^{11}	1.4400×10^{11}
$\boldsymbol{R_s}$ [Ω]	9.882 [9.68, 10.02]	9.809 [9.22, 10.30]
$\boldsymbol{R_{ct}}$ [Ω]	100.323 [99.96, 100.84]	100.565 [99.71, 101.55]
$\boldsymbol{Q}$ [μF s^{n-1}]	9.943 [9.538, 10.465]	10.390 [9.044, 11.758]
$\boldsymbol{n}$ [–]	0.900 [0.89, 0.90]	0.894 [0.88, 0.91]
$\boldsymbol{\sigma}$ [Ω $s^{-1/2}$]	1.0000×10^{-1} [1.0000×10^{-6}, 1.0000×10^{-1}]	3.1800×10^{-4} [1.0000×10^{-6}, 1.0000×10^{-1}]

Values in brackets: 95% confidence intervals. Q is reported in μF s^{n-1}; n is dimensionless; σ is reported in Ω $s^{-1/2}$. Bold entries (RMSE, AIC, BIC, Cond#, and circuit parameters) indicate the key fitting metrics and estimated model parameters highlighted in the discussion.

4.7. Global Model Comparison

Table 8 summarizes the key fitting metrics for all seven evaluated models at both noise levels. At 2.5% , differences in *RMSE* among the more complex models (Randles full, Randles+Warburg, $(R_{ct} + Z_W) \parallel$ CPE) are marginal, with statistical improvements in *AIC* and *BIC* insufficient to justify overparameterization when σ or n exhibit broad confidence intervals or strong collinearity. At 5.0% noise, the more parsimonious models (Randles+CPE and $(R_{ct} + Z_W) \parallel$ CPE) yield lower *AIC*/*BIC* values with negligible R^2 loss, reflecting greater robustness against signal degradation.

From a physical standpoint, the simultaneous inclusion of a CPE and Warburg impedance (Randles full) is warranted only when the spectrum exhibits quantifiable evidence of both interfacial non-ideality and semi-infinite diffusion, and when the spectral range adequately excites both processes. In the absence of these conditions, partial models offer a superior trade-off between fitting fidelity, parameter stability, and parsimony.

Table 8. Comparative summary of fitting metrics for all evaluated models. Bold values indicate the best performance for each metric and noise level.

Model	**2.5%**			**5.0%**		
	RMSE	**AIC**	**BIC**	**RMSE**	**AIC**	**BIC**
RLC series	4.10	380	396	7.20	385	402
Randles classic	3.45	355	370	6.80	362	379
Randles + CPE	3.30	352	369	**6.50**	**354**	**372**
Randles + Warburg	**3.25**	**349**	368	6.60	358	378
$(R_{ct} + Z_W) \parallel C_{dl}$	3.28	351	**367**	6.55	355	373
$(R_{ct} + Z_W) \parallel$ CPE	3.27	350	368	6.53	355	374
Randles full	3.27	350	369	6.62	356	376

Bold entries indicate the best performance for each metric and noise level across the evaluated models.

5. Conclusions

This work establishes a fully integrated and analytically rigorous framework for Electrochemical Impedance Spectroscopy (EIS) analysis, combining exact impedance formulations, closed-form Jacobians, hybrid global–local optimization, and exhaustive statistical

validation. Applied consistently across seven representative equivalent circuit models under controlled synthetic conditions, the methodology delineates precise statistical and physical boundaries for model applicability, bridging the gap between theoretical formulation and practical implementation.

Results demonstrate that the classical Randles circuit remains the most parsimonious and statistically optimal choice for systems with ideal charge-transfer kinetics and capacitive behavior, while configurations incorporating Constant Phase Elements (CPE) and Warburg diffusion elements provide superior fidelity for heterogeneous or diffusion-limited interfaces. The robustness of R_{ct} estimation across noise levels, alongside the ability to quantify non-ideal capacitive parameters and diffusive amplitudes, underscores the stability and reproducibility of the approach.

Critically, automated Kramers–Kronig compliance testing ensures that all fitted spectra satisfy the fundamental principles of linearity and causality, eliminating a recurrent source of interpretative bias in the EIS literature. The modularity of the platform enables rapid extension to novel circuit topologies, integration with experimental datasets, and coupling with advanced electrochemical-transport models.

By uniting analytical precision, computational efficiency, and rigorous statistical scrutiny, this framework delivers an unprecedented level of objectivity in EIS model selection and parameter interpretation. As such, it is positioned to become a reference standard for quantitative EIS analysis, setting a reproducible benchmark for the accurate characterization and optimization of electrochemical systems in energy storage, corrosion science, and electrocatalysis.

From a practical standpoint, the proposed methodology can assist experimentalists and industry practitioners in rapidly discriminating between competing mechanistic hypotheses, improving the reliability of diagnostics and the efficiency of device optimization workflows. In general, simpler models are preferable for datasets with low noise and well-defined features, whereas more complex models should only be adopted when the spectra exhibit clear evidence of non-ideal capacitive behavior or diffusive transport, ensuring parsimony without sacrificing fidelity.

Funding: The APC was funded by Universidad Politécnica de Lázaro Cárdenas (UPLC), Michoacán, Mexico.

Institutional Review Board Statement: Not applicable.

Informed Consent Statement: Not applicable.

Data Availability Statement: The full Python implementation (`eis.py`) is openly available at Zenodo (https://doi.org/10.5281/zenodo.17109696). This ensures reproducibility and facilitates adaptation of the methodology by other researchers. Further clarifications regarding the implementation can be obtained by contacting the corresponding author at the email address provided in the manuscript.

Acknowledgments: I sincerely appreciate the Universidad Politécnica de Lázaro Cárdenas for offering me the opportunity and the essential resources to carry out this project.

Conflicts of Interest: The author declares no conflicts of interest.

Abbreviations

The following abbreviations are used in this manuscript:

AIC	Akaike Information Criterion
BIC	Bayesian Information Criterion
CI	Confidence interval
CPE	Constant-phase element

AIC	Akaike Information Criterion
BIC	Bayesian Information Criterion
CI	Confidence interval
CPE	Constant-phase element
DE	Differential Evolution
DRT	Distribution of relaxation times
ECM	Equivalent circuit model
EIS	Electrochemical impedance spectroscopy
KK	Kramers–Kronig
LM	Levenberg–Marquardt
LTI	Linear time-invariant
RMSE	Root-mean-square error
RLC	Resistor–Inductor–Capacitor
C_{dl}	Double-layer capacitance
R_{ct}	Charge-transfer resistance
R_s	Solution resistance
Z_W	Warburg (semi-infinite diffusion) impedance

References

1. Magar, H.S.; Hassan, R.Y.; Mulchandani, A. Electrochemical impedance spectroscopy (EIS): Principles, construction, and biosensing applications. *Sensors* **2021**, *21*, 6578. [CrossRef]
2. Lazanas, A.C.; Prodromidis, M.I. Electrochemical impedance spectroscopy—A tutorial. *ACS Meas. Sci. Au* **2023**, *3*, 162–193. [CrossRef]
3. Perry, D.; Mamlouk, M. Probing mass transport processes in Li-ion batteries using electrochemical impedance spectroscopy. *J. Power Sources* **2021**, *514*, 230577. [CrossRef]
4. Harrington, D.A.; Van den Driessche, P. Mechanism and equivalent circuits in electrochemical impedance spectroscopy. *Electrochim. Acta* **2011**, *56*, 8005–8013. [CrossRef]
5. Maksoud, M.A.; Bekhit, M.; Waly, A.L.; Awed, A.S. Optical and dielectric properties of polymer nanocomposite based on PVC matrix and Cu/Cu_2O nanorods synthesized by gamma irradiation for energy storage applications. *Phys. E Low-Dimens. Syst. Nanostructures* **2023**, *148*, 115661. [CrossRef]
6. Van Haeverbeke, M.; Stock, M.; De Baets, B. Equivalent electrical circuits and their use across electrochemical impedance spectroscopy application domains. *IEEE Access* **2022**, *10*, 51363–51379. [CrossRef]
7. Gateman, S.M.; Gharbi, O.; De Melo, H.G.; Ngo, K.; Turmine, M.; Vivier, V. On the use of a constant phase element (CPE) in electrochemistry. *Curr. Opin. Electrochem.* **2022**, *36*, 101133. [CrossRef]
8. Randviir, E.P.; Banks, C.E. A review of electrochemical impedance spectroscopy for bioanalytical sensors. *Anal. Methods* **2022**, *14*, 4602–4624. [CrossRef] [PubMed]
9. Esser, M.; Rohde, G.; Rehtanz, C. Electrochemical impedance spectroscopy setup based on standard measurement equipment. *J. Power Sources* **2022**, *544*, 231869. [CrossRef]
10. Barbero, G.; Batalioto, F.; Figueiredo Neto, A.M.; Lelidis, I. Deviations from linearity in impedance spectroscopy measurements confirmed by Kramers–Kronig analysis. *Electrochim. Acta* **2021**, *388*, 139277. [CrossRef]
11. Zhang, R.; Black, R.; Sur, D.; Karimi, P.; Li, K.; DeCost, B.; Hattrick-Simpers, J. Editors' choice—AutoEIS: Automated Bayesian model selection and analysis for electrochemical impedance spectroscopy. *J. Electrochem. Soc.* **2023**, *170*, 086502. [CrossRef]
12. Nuñez Perez, F.A. Electrochemical analysis of corrosion resistance of manganese-coated annealed steel: Chronoamperometric and voltammetric study. *AppliedChem* **2024**, *4*, 367–383. [CrossRef]
13. Núñez-Perez, F.A. Electrochemical analysis of the corrosion resistance of annealed steel with nickel coating in marine environment simulations: Chronoamperometric and voltammetric study. *Ibero-Am. J. Eng. Technol. Stud.* **2024**, *4*, 62–70. [CrossRef]
14. Davey, S.B.; Cameron, A.P.; Latham, K.G.; Donne, S.W. Combined step potential electrochemical spectroscopy and electrochemical impedance spectroscopy analysis of the glassy carbon electrode in an aqueous electrolyte. *Electrochim. Acta* **2021**, *396*, 139220. [CrossRef]
15. Chen, C.-C.; Hung, C.-H.; Zhu, H.-X.; Chen, J.-Z. High-sensitivity electrical admittance sensor with regression analysis for measuring mixed electrolyte concentrations. *Sensors* **2024**, *24*, 7379. [CrossRef] [PubMed]
16. López-Villanueva, J.A.; Rodríguez Bolívar, S. Constant phase element in the time domain: The problem of initialization. *Energies* **2022**, *15*, 792. [CrossRef]

17. Wang, L.; Song, Z.; Zhu, L.; Jiang, J. Fast electrochemical impedance spectroscopy of lithium-ion batteries based on the large square wave excitation signal. *iScience* **2023**, *26*, 106531. [CrossRef]
18. Caeiro, A.; Canhoto, J.; Rocha, P.R. Electrochemical impedance spectroscopy as a micropropagation monitoring tool for plants: A case study of tamarillo (*Solanum betaceum*) callus. *iScience* **2025**, *28*, 109123. [CrossRef]
19. Berliner, M.D.; Jiang, B.; Cogswell, D.A.; Bazant, M.Z.; Braatz, R.D. Novel operating modes for the charging of lithium-ion batteries. *J. Electrochem. Soc.* **2022**, *169*, 100546. [CrossRef]
20. Suárez-Herrera, M.F.; Scanlon, M.D. On the non-ideal behaviour of polarised liquid–liquid interfaces. *Electrochim. Acta* **2019**, *328*, 135110. [CrossRef]
21. Silva, T.R.; Araújo, A.J.M.; Raimundo, R.A.; Ferreira, L.S.; Macedo, D.A.; Marques, P.A.A.P.; Loureiro, F.J.A.; Fagg, D.P. One-step fabrication of self-supported $MnCo_2O_4$-reduced graphene oxide-based anodes for the alkaline oxygen evolution reaction. *J. Phys. Chem. Solids* **2026**, *208*, 113067. [CrossRef]
22. Ammar, N.; Vincent, D. Design and analysis of two layers RLC network of rectangular topology by wave concept iterative process method. *Int. J. Numer. Model. Electron. Netw. Devices Fields* **2020**, *33*, e2805. [CrossRef]
23. Schalenbach, M.; Raijmakers, L.; Tempel, H.; Eichel, R.A. How microstructures, oxide layers, and charge transfer reactions influence double layer capacitances. Part 2: Equivalent circuit models. *Electrochem. Sci. Adv.* **2025**, *5*, e202400010. [CrossRef]
24. Patel, B.; Sorrentino, A.; Vidakovic-Koch, T. Data-driven analysis of electrochemical impedance spectroscopy using the Loewner framework. *iScience* **2025**, *28*, 109987. [CrossRef]
25. Orazem, M.E.; Ulgut, B. On the proper use of a Warburg impedance. *J. Electrochem. Soc.* **2024**, *171*, 040526. [CrossRef]
26. van den Bergh, W.; Stefik, M. Understanding rapid intercalation materials one parameter at a time. *Adv. Funct. Mater.* **2022**, *32*, 2204126. [CrossRef]

Disclaimer/Publisher's Note: The statements, opinions and data contained in all publications are solely those of the individual author(s) and contributor(s) and not of MDPI and/or the editor(s). MDPI and/or the editor(s) disclaim responsibility for any injury to people or property resulting from any ideas, methods, instructions or products referred to in the content.